NUCLEAR REACTIONS -- THEORY

IMAGING OF SOURCES IN HEAVY–ION REACTIONS

David A. Brown and Paweł Danielewicz

In astronomy, phase interferometry [1] is used to image star surfaces, e.g. Betelgeuse [2]. Intensity interferometry is primarily used to determine radii of stars in astronomy to to determine radii of particle emitting regions in heavy-ion reactions. In heavy-ion reactions, this is most often done by fitting the low-momentum two-particle correlation functions under the assumption of Gaussian-shaped emitting regions [3]. Similarly, source lifetimes have been inferred by considering Gaussian-shaped distributions of emission times. Beyond this, no attempts have been made to image the source function from the reaction data. Typically, comparison to reaction simulations is carried out by generating the correlation functions from simulated events.

We have investigated the feasibility of direct imaging of the source from reaction data using intensity interferometry. Given a two-particle correlation function, this is an inversion problem. We illustrate two examples: that of like-charged-pion and that of proton-proton interferometry. In the like-pion case, the relative source function is a Fourier transformation of the two-particle correlation function. In the proton case, the procedure is more involved. In this report, we discuss the relation of the correlation function to the source function and how the imaging is performed.

Assuming that processes leading to two particles in the final state are approximately independent and assuming that the product of single-particle sources has a weak dependence on momenta important for correlations, the two-particle correlation function may be written as [4, 5]

$$C_{\mathbf{P}}(\mathbf{q}) = \frac{dN_2/d\mathbf{p}_1\, d\mathbf{p}_2}{(dN_1/d\mathbf{p}_1)\,(dN_1/d\mathbf{p}_2)} \simeq \int d\mathbf{r}\, |\Phi_{\mathbf{q}}^{(-)}(\mathbf{r})|^2\, S_{\mathbf{P}}(\mathbf{r}). \tag{1}$$

Here $S_{\mathbf{P}}(\mathbf{r})$ is the relative distribution of emission points for two particles with similiar momenta, in their center of mass. Here also, $\Phi_{\mathbf{q}}^{(-)}(\mathbf{r})$ is the two–particle relative wavefunction with outgoing boundary conditions. For like particles, S is a symmetric function. This is not generally the case for distinct particles. Depending on the circumstances in a reaction, S may range from isotropic, for prompt emission, to strongly elongated along $\mathbf{P}$.

With Eq. (1), the goal of the imaging is to determine S given C. Given that the interesting part of the correlation function is its deviation from 1, we subtract 1 from both sides of (1) obtaining

$$C_{\mathbf{P}}(\mathbf{q}) - 1 = \int d\mathbf{r}\, \left(|\Phi_{\mathbf{q}}^{(-)}(\mathbf{r})|^2 - 1 \right) S_{\mathbf{P}}(\mathbf{r}) = \int d\mathbf{r}\, K(\mathbf{q},\mathbf{r})\, S_{\mathbf{P}}(\mathbf{r}), \tag{2}$$

where $K = |\Phi_{\mathbf{q}}^{(-)}|^2 - 1$. The problem of imaging then reduces to inverting K.

Now we find the angular moments of the source and the correlation function. The directions that we use in this analysis are, in the system frame, outward along the transverse momentum of the pair, longitudinal along the beam, and transverse direction which is perpindicular to these two directions. First we introduce $C(\mathbf{q}) = \sqrt{4\pi} \sum_{\lambda m} C^{\lambda m}(q)\, \mathrm{Y}^{\lambda m}(\Omega_{\mathbf{q}})$ and an analogous representation for S. Next, since the spin-averaged operator, K, only depends on the angle between $\mathbf{q}$ and $\mathbf{r}$, it may be expanded:

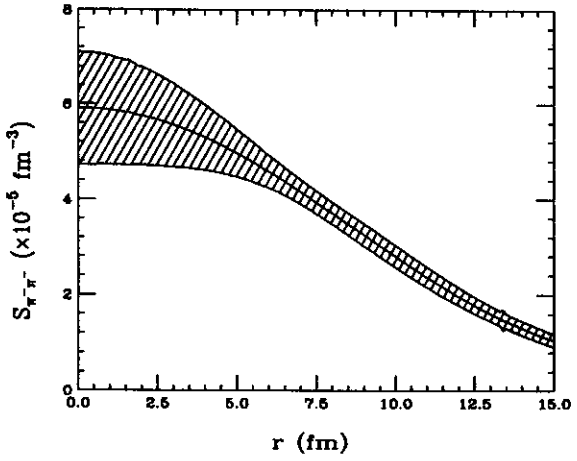

Figure 1: Relative distribution of emission points for π^- determined from the correlation data of Ref. [7]. The shaded area represents uncertainty in the source function associated with the uncertainty in the determination of the π^- correlation function [7] and due to the choice of $q_{\rm max} \approx 50$ MeV/c.

$K(\mathbf{q},\mathbf{r}) = \sum_\lambda (2\lambda+1)\, K_\lambda(q,r)\, P^\lambda(\cos\theta)$. A relation between the moments follows from (2),

$$C_{\mathbf{P}}^{\lambda m}(q) - \delta^{\lambda 0}\,\delta^{m0} = 4\pi \int_0^\infty dr\, r^2\, K_\lambda(q,r)\, S_{\mathbf{P}}^{\lambda m}(r)\,. \tag{3}$$

Due to the symmetry of S and C, only even λ appear in the angular expansion of these functions. Since both functions are real, the moments satisfy $(C^{\lambda m})^* = (-1)^m\, C^{\lambda\, -m}$. Relation (3) between the angular moments may help in analyzing the three-dimensional data. In particular, this relation shows that the angle-averaged correlation function $C^{00}(q) \equiv C(q)$ reflects the angle-averaged source $S^{00}(r) \equiv S(r)$. For the like–nucleon and like–charged–pion cases, the $\lambda = 0$ operator is

$$K_0(q,r) = \frac{1}{2} \sum_{j s \ell \ell'} (2j+1)\, \left(g_{j s}^{\ell \ell'}(r)\right)^2 - 1\,, \tag{4}$$

where $g_{j s}^{\ell \ell'}$ is the radial wave function with outgoing asymptotic angular momentum ℓ.

For like-pion pairs, ignoring the interactions between the pions, K in Eq. (2) is $K(\mathbf{q},\mathbf{r}) = \cos(2\mathbf{q}\cdot\mathbf{r})$. This is a Fourier cosine transform. Given that S is symmetric, this Fourier transform can be inverted. Doing so, we arrive at the equation for the angle–averaged correlation function and source:

$$r\, S_{\mathbf{P}}(r) = \frac{2}{\pi^2} \int_0^\infty dq\, q\, \sin(2qr)\, (C_{\mathbf{P}}(q) - 1)\,. \tag{5}$$

As a specific example of source extraction, in Fig. 1 we present the relative angle-averaged π^- source-function. It is determined by applying Eq. (5) to the data of Ref. [7] for central 10.8 GeV/c Au + Au. Prior to the Fourier transformation in Eq. (5), the data were corrected for the Coulomb interaction between the two pions and between the pions and the source [6]. The integration in (5) for Fig. 1 was cut off at $q_{\rm max} \simeq 50$ MeV/c, giving a resolution in the relative distance in the figure of $\Delta r \sim 1/2q_{\rm max} \sim 2.0$ fm.

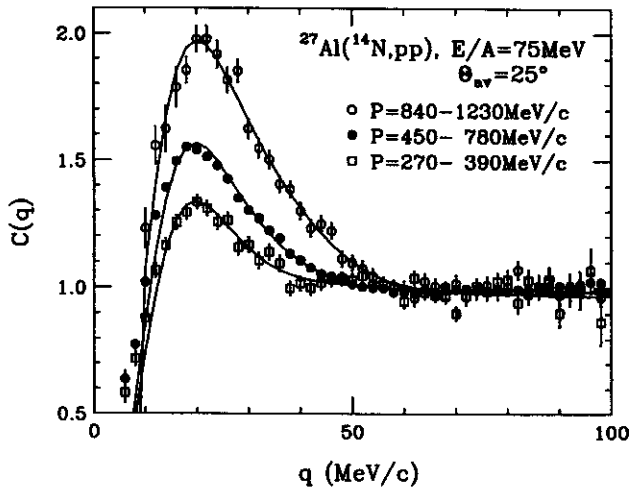

Figure 2: Two-proton correlation function for the ^{14}N + ^{27}Al reaction at 75 MeV/nucleon. The symbols represent data [9, 8] for three gates of total momentum imposed on protons emitted in the vicinity of $\theta_{\rm lab} = 25°$. The lines represent the correlation function for the extracted sources displayed in Fig. 3.

The like–nucleon operator, K, may not be inverted so simply. In this case, we determine the source by first discretizing the functions and integrals in, for example, Eq. (3) for $\lambda = m = 0$:

$$C_{\rm P}(q) - 1 \simeq \sum_k w_k(q)\, S_{\rm P}(r_k)\,. \tag{6}$$

Here $w_k(q)$ is the discretized $K_0(q,r)$ operator and $r_k = (k - \frac{1}{2})\Delta r$. We then minimize $\chi^2_{\rm P} = \sum_j ((C^{\rm exp}_{\rm P}(q_j) - C_{\rm P}(q_j))/\sigma_j)^2$ by varying $S(r_k)$, subject to the conditions that $S(r_k) \geq 0$ and that S is normalized to 1.

We illustrate this technique by analyzing the angle–averaged proton-proton correlation data [8, 9] from the 75 MeV/nucleon ^{14}N + ^{27}Al reaction, displayed in Fig. 2. We chose to fit within the region $q_{\rm max} \simeq 80$ MeV/c$> q > q_{\rm min} = 10$ MeV/c to avoid various experimental and theoretical complications [10, 9]. This gives us a resolution of $\Delta r = 1.8$ fm. We determine the pp wavefunctions for $\ell, \ell' \leq 2$ from the Schrödinger equation with the regularized Reid soft-core potential [11]. Initially, we aimed to determine the source up to $r_{\rm max} \sim 30$ fm, but we found that the fits favored S consistent with zero at higher r. Thus, we were able to reduce $r_{\rm max}$ to 16.2 fm without an appreciable worsening in the fits.

The source functions extracted from the data [8, 9] are shown for the three total-momentum gates in Fig. 3 together with the source functions determined directly within Boltzmann-equation reaction-simulations [12, 8]. The errors on the extracted S include the uncertainty from varying $q_{\rm max}$ in the vicinity of 80 MeV/c. The values of χ^2 per degree of freedom are 1.1 for the highest momentum gate, 1.8 for the lowest, and 4.9 for the intermediate one with the lowest errors on the data. The change in the relative distribution of emission points in Fig. 3, from a compact form at high proton momenta to an extended form at low momenta, demonstrate the presence of space-momentum correlations within the ^{14}N + ^{27}Al reaction. At intermediate and low momenta, neither the relative proton distributions from the data, nor those from the model, can be well approximated by Gaussians. This is in contrast to the distribution in Fig. 1, and to a degree, to distributions for high momenta in Fig. 3. Overall, the transport model yields distributions in a near-quantitative agreement with the experimental sources. The model source seems to systematically underestimate the values from the data only at the shortest r.

We have shown how to determine the relative source functions for particles directly from correlation data using either direct Fourier inversion or fitting of the source. Currently, we are adapting other

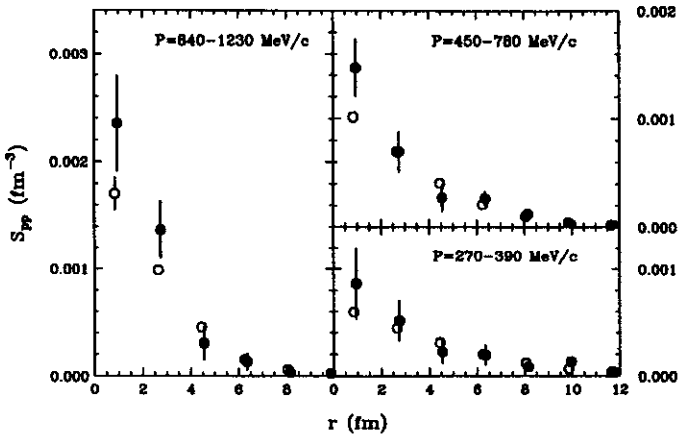

Figure 3: Relative source function for protons emitted from the $^{14}N + ^{27}Al$ at 75 MeV/nucleon, in the vicinity of $\theta_{lab} = 25°$, within three total momentum intervals. Filled circles represent the function extracted from the data [9, 8]. Open circles represent the function determined within the Boltzmann-equation model [13].

image processing techniques such as the Maximum Entropy Method [13] to the problem of extracting sources from correlation data.

References

1. J. T. Armstrong *et al.*, Physics Today 48, 42 (1995).
2. D. Buscher *et al.*, Mon. Not. R. Astro. Soc. 245, 7p (1990).
3. D. H. Boal, C. K. Gelbke, and B. K. Jennings, Rev. Mod. Phys. 62, 553 (1990).
4. S. Pratt, T. Csörgö, and J. Zimányi, Phys. Rev. C 42, 2646 (1990).
5. P. Danielewicz and P. Schuck, Phys. Lett. B 274, 268 (1992).
6. G. Baym and P. Braun-Munzinger, report nucl-th/9606055, 1996.
7. D. Miśkowiec (E877 Collaboration), Nucl. Phys. A610 (1996).
8. W. G. Gong *et al.*, Phys. Rev. C 47, R429 (1993).
9. W. G. Gong *et al.*, Phys. Rev. C 43, 1804 (1991).
10. B. Kämpfer *et al.*, Phys. Rev. C 48, R955 (1993).
11. V. G. J. Stoks *et al.*, Phys. Rev. C 49, 2950 (1994).
12. P. Danielewicz, Phys. Rev. C 51, 716 (1995).
13. C. R. Smith and W. T. Grandy, *Maximum-Entropy and Bayesian Methods in Inverse Problems* (D. Reidel Publishing Co., Dordrecht, 1985).

MANY-BODY COULOMB PERTURBATION OF AZIMUTHAL α-α CORRELATIONS

R. Popescu, C.K. Gelbke and T. Glasmacher

Particles emitted in intermediate-energy heavy-ion collisions are known to exhibit strong azimuthal anisotropies [1-4]. These anisotropies are generally associated with a collective velocity component of the emitted particles with respect to the orientation of the entrance channel reaction plane. Azimuthal correlations reflecting rotational motion become less pronounced for increasing beam energy and for small-impact parameter collisions [1] selected by cuts on large charged-particle multiplicities N_C, or total transverse energy E_t.

Decreasing azimuthal anisotropies might, however, also arise from Coulomb distortions in the field of the emitting nucleus and the randomization of the velocity components due to many-body Coulomb interactions between emitted particles. In this analysis, we investigate this issue via classical many-body Coulomb trajectory calculations for the simple case of an instantaneous release of all emitted particles from the surface of the emitting source using as initial velocity distribution that of a rotating hot gas [2].

We adopt a simple classical model [2] for an instantaneous particle emission from the surface of a sphere containing a hot gas of nucleons and clusters. The parameters of the model are the radius R of the source, its angular velocity ω, and its temperature T. The initial emission pattern from this source is parametrized as [2]

$$\frac{d^5N}{dS \cdot d^3v} \propto (\hat{n} \cdot \vec{v}) \cdot \exp\left\{-\frac{m\left(v^2 - 2R\omega v \sin\theta' \sin\phi' \sin\alpha\right)}{2T}\right\} . \tag{1}$$

Here, v and m denote the velocity and mass of the emitted particle; dS denotes the surface element with normal $\hat{n}$; α is the angle between the axis of rotation $\vec{\omega}$ and the velocity vector $\vec{v}$; θ' and ϕ' denote the polar and azimuthal coordinates of the surface normal $\hat{n}$ for a coordinate system in which the polar (z') axis is parallel to the velocity vector $\vec{v}$ and the plane (x', z') contains the rotation axis $\vec{\omega}$. Our choice of laboratory coordinate system is such that the beam axis is parallel to the z-axis and the angular velocity vector is located in the (x,y)-plane; the reaction plane is defined as the plane perpendicular to $\vec{\omega}$ which contains the beam axis. With this choice of coordinate system,

$$\sin\alpha = \sqrt{1 - \sin^2\theta \sin^2\phi} , \tag{2}$$

where θ is the polar angle of the emitted particle with respect to the beam axis and ϕ is the azimuthal angle, with $\phi = 0°$ or $\phi = 180°$ indicating emission in the reaction plane.

Integration over the surface of the emitting source gives the emission pattern for a rotating classical gas [2],

$$\frac{d^3N}{dE \cdot d\Omega} \propto E \cdot e^{-E/T} \cdot \frac{J_1\left(iA\sqrt{E - E\sin^2\theta\sin^2\phi}\right)}{iA\sqrt{E - E\sin^2\theta\sin^2\phi}} , \tag{3}$$

where J_1 is the first-order Bessel function and

$$A = \sqrt{2m} \cdot \omega R/T \,. \tag{4}$$

We have chosen source parameters which provide transverse energy spectra and particle distributions which resemble those measured for $^{36}Ar + ^{197}Au$ collisions at $E/A = 35MeV$ [3]. Specifically we used the parameters $R = 10fm$, $\omega R = 0.1c$ and $T = 9MeV$. The element distribution of intermediate mass fragments (IMF: $Z_{IMF} \geq 3$) was assumed to have an exponential probability distribution. The mass number, A_{IMF}, was assumed to be that of the most abundant isotope of charge number Z_{IMF}.

Calculations were performed for fixed charged particle multiplicity N_C. For $Z_{emit} < Z_{tot}$, a source residue of charge $Z_{res} = Z_{tot} - Z_{emit}$ was assumed to be formed. Momentum conservation was established by balancing the total momentum of the emitted charged particles, $\mathbf{P}_{emit}$, with the momentum of the remaining system.

After having chosen the particles for a given event, their initial positions at the surface of the emitting source and their initial velocities, all particles were assumed to be released at the same time. Their trajectories were then evolved by numerically solving the classical equations of motion under their mutual Coulomb forces. Relativistic effects were neglected. In most calculations, the finite size of the emitted particles was ignored, and the particles were treated as classical point particles. The exclusion of initial conditions in which two particles were separated by a distance less than $d_{min} = 1.2 \cdot (A_1^{1/3} + A_2^{1/3})$ leads to slightly attenuated azimuthal correlations at large multiplicities. To isolate the effects solely due to Coulomb final-state interactions, we ignored this multiplicity-dependent geometrical complication, as well as a possible dependence of the source radius on N_C.

In the following, we restrict the discussion to many-body Coulomb distortions calculated for emitted α-particles. This choice was justified by the facts that α-particles are emitted with large cross sections and that they are sufficiently heavy to exhibit clear signatures of the underlying collective motion [3]. Energies and angles of the emitted particles will be given in the center of mass frame of reference.

As can be qualitatively expected, many-body Coulomb distortions are more pronounced for particles emitted with lower energy than for particle emitted with higher energy. This effect is illustrated in Fig. 1. The figure compares unperturbed (curves) and perturbed (for $N_C = 40$, points) azimuthal distributions of α-particles emitted at $\theta = 70° - 110°$ with energies $E_\alpha < E_0$ (open points and dashed curve) and $E_\alpha > E_0$ (solid points and solid curve). Because of the $(E \sin^2\theta \sin^2\phi)$-dependence in Eq. (3), emission in the reaction plane is less pronounced at smaller angles than at $\theta = 90°$. In order to account for the acceleration in the Coulomb field of the source, we have taken E_0 = 30 and 60 MeV for the unperturbed (no Coulomb) and perturbed (with Coulomb) distributions, respectively. Azimuthal distributions of *energetic* particle thus offer the advantages of enhanced in-plane emission [3] *and* reduced perturbation of this emission pattern from many-body Coulomb interactions.

Azimuthal distributions with respect to the true reaction plane, such as those shown in Fig. 1, cannot be directly observed because the orientation of the reaction plane cannot be accurately determined on an event-by-event basis. Azimuthal two-particle correlation functions exhibit a strong sensitivity to the azimuthal distribution of emitted particles, but they do not require the reconstruction of the reaction plane and allow therefore a more direct comparison between theory and experiment.

Azimuthal correlation functions are defined as the ratio of the two-particle coincidence yield over a suitably chosen background yield. We construct azimuthal two-particle correlation functions from events

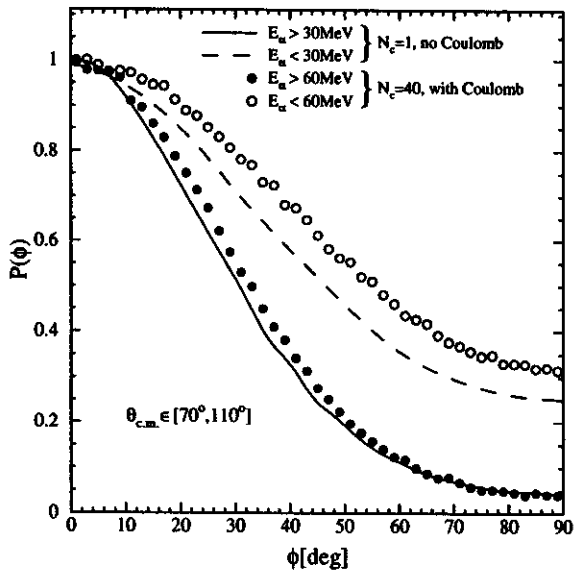

Figure 1: Azimuthal distribution with respect to the reaction plane for α-particles emitted at $\theta = 70° - 110°$. The solid (open) points and solid (dashed) curve show distributions for high, $E_\alpha > E_0$, (low, $E_\alpha < E_0$) energy α-particles, respectively. Curves show unperturbed distributions ($N_C = 1$, no Coulomb); points show distortions for $N_C = 40$.

of fixed charged particle multiplicity according to the definition

$$1 + R(\Delta\phi_{\alpha\alpha}) = C \cdot \frac{\sum_i Y^i_{\alpha\alpha}(\theta_1, \phi_1, \theta_2, \phi_2)}{\sum_{i \neq k} Y^i_\alpha(\theta_1, \phi_1 + \Phi_i) \cdot Y^k_\alpha(\theta_2, \phi_2 + \Phi_k)} \,. \tag{5}$$

In Eq. (5), C is a normalization constant; the labels i and k denote individual events; Φ_i and Φ_k are randomly chosen orientations of the reaction planes for events i and k; sum in the numerator extends over all events i and all coincident pairs of α-particles within a given bin of $\Delta\phi_{\alpha\alpha} = |\phi_1 - \phi_2|$ (defined over the interval $[0°, 180°]$) and selected by specified constraints on E_α and θ. In analogy, the sum in the denominator extends over all pairs of α-particles from different events i and k within the corresponding bin, $\Delta\phi_{\alpha\alpha} = |\phi_1 + \Phi_i - \phi_2 - \Phi_k|$, and selected by the given constraints on E_α and θ. Correlation functions shown in Figs. 2-3 have been normalized by their integral over the interval $\Delta\phi_{\alpha\alpha} \in [90°, 180°]$.

Energy integrated azimuthal two-α-particle correlation functions for $\theta = 70° - 110°$ are shown in Fig. 2. The solid curve shows the initial (unperturbed) correlation function for $N_C = 10$, without final-state interactions. This correlation function exhibits the well known V-shape of the two-particle distribution which arises from the in-plane enhancement of the single-particle emission pattern [2]. The dotted, dashed, and dot-dashed curves show correlation functions modified by many-body final-state Coulomb interactions for N_C = 10, 20 and 40, respectively. The amplitude of the V-shaped modulation of the correlation function decreases for large values of N_C. In addition, the two-α-particle correlation function exhibits a pronounced minimum at $\Delta\phi_{\alpha\alpha} = 0°$ ("Coulomb hole") which is caused by Coulomb repulsion

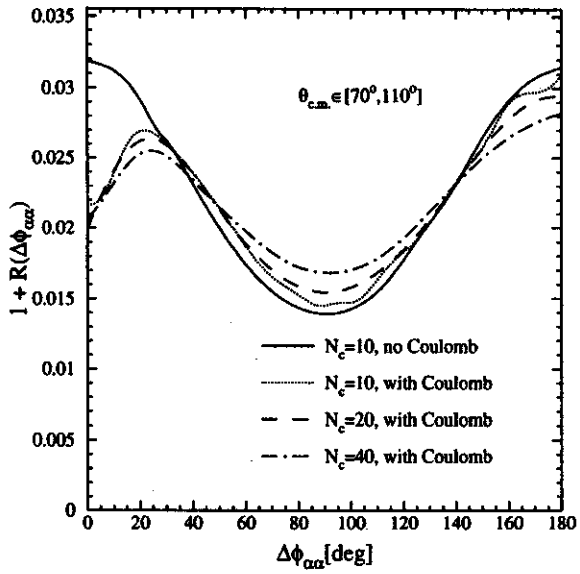

Figure 2: Energy integrated azimuthal two-α-particle correlation functions, $1+R(\Delta\phi_{\alpha\alpha})$, for α-particles emitted at $\theta = 70° - 110°$. The solid curve shows the unperturbed correlation function for $N_C = 10$. The dotted, dashed, and dot-dashed curves show correlation functions modified by many-body final-state Coulomb interactions for $N_C = 10$, 20, and 40, respectively.

between the two coincident α-particles. As was already pointed out in ref. [4], the magnitude of this minimum depends on the space-time characteristics of the emitting source.

The magnitude and detailed shape of the minimum at $\Delta\phi_{\alpha\alpha} = 0°$ depend on the charged particle multiplicity. This effect is primarily due to the many-body distortion of the single-particle emission pattern with respect to the reaction plane, which leads to a multiplicity-dependent attenuation of the V-shaped azimuthal correlation pattern. Since in the calculations the orientation of the reaction plane is known, this V-shaped "background" pattern can be eliminated by turning off the Φ-randomization in the calculation of the background correlation function. Setting $\Phi_i = \Phi_k = 0°$ in Eq. (5), one can construct a correlation function, $1 + R_{\Phi=0°}(\Delta\phi_{\alpha\alpha})$, for fixed orientation of the reaction plane. This correlation function, shown in Fig. 3, exhibits a clear minimum at $\Delta\phi_{\alpha\alpha} = 0°$ and is flat at large angles, but its shape is rather insensitive to the assumed value of N_C. Such an insensitivity follows from the Koonin-Pratt formula [5] which implies that two-particle correlation functions at small relative momenta are sensitive to the space-time geometry of the emitting source, but not to the multiplicity of emitted particles – as long as the correlation function is dominated by the interaction between the two detected particles. The calculated insensitivity of the small-angle behavior of $R_{\Phi=0°}(\Delta\phi_{\alpha\alpha})$ to N_C then indicates that perturbations of the Coulomb hole by interactions with other particles are small.

In order to summarize the modifications of the two-α-particle azimuthal correlation functions at large angles, we have fit the correlation functions, $1 + R(\Delta\phi_{\alpha\alpha})$, by a simple functional form,

$$1 + R(\Delta\phi_{\alpha\alpha}) = a_0(1 + a_2 \cos 2\Delta\phi_{\alpha\alpha}) \,, \tag{6}$$

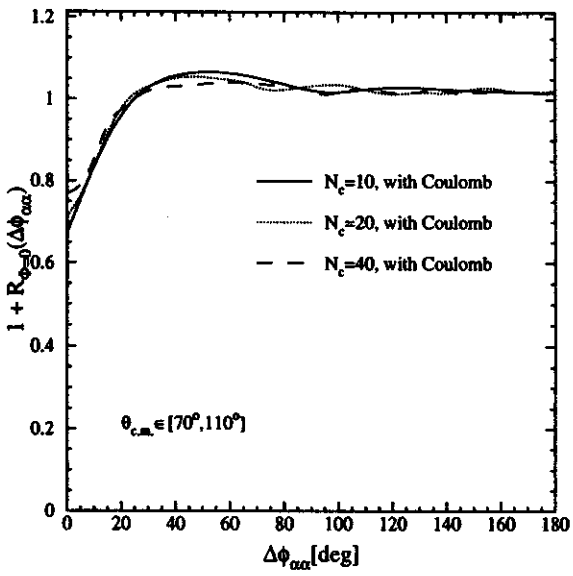

Figure 3: Energy integrated correlation function, $1 + R_{\Phi=0°}(\Delta\phi_{\alpha\alpha})$, for fixed orientation of the reaction plane and for α-particles emitted at $\theta = 70° - 110°$. The solid, dotted, and dashed curves show correlation functions modified by many-body final-state Coulomb interactions for $N_C = 10$, 20, and 40, respectively.

and constrained the fit to angles $\Delta\phi_{\alpha\alpha} > 45°$.

Figure 4 shows the N_C-dependence of the parameter a_2, extracted from the azimuthal correlation functions of two α-particles emitted at $\theta = 70° - 110°$. Circular points show values extracted for energy-integrated correlation functions. Triangle and square shaped points represent results for low ($E_\alpha < E_0$) and high ($E_\alpha > E_0$) energy α-particles, respectively. As before, E_0 = 30 and 60 MeV for the cases without and with Coulomb acceleration, respectively. Open and solid points represent unperturbed and perturbed correlations function, respectively. For the cases investigated, the parameter a_2 exhibits a monotonic attenuation as a function of N_C. The relative magnitude of this attenuation is most pronounced for low-energy particles and become insignificant for high-energy particles.

References

1. L. Phair *et al.*, Nucl. Phys. A564, 453 (1993).
2. C.B. Chitwood *et al.*, Phys. Rev. C 34, 858 (1986).
3. M.B. Tsang *et al.*, Phys. Rev. C 44, 2065 (1991).
4. T. Ethvignot *et al.*, Phys. Rev. C 46, 637 (1992).
5. S.E. Koonin, Phys. Rev. Lett. 70B, 43 (1977).

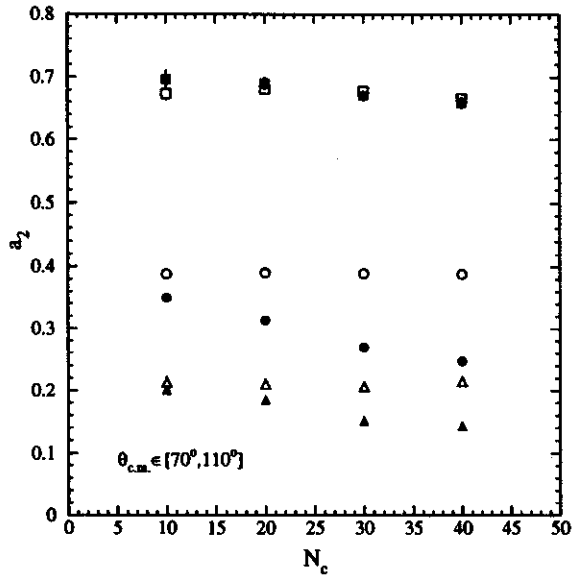

Figure 4: Dependence of the parameter a_2 on the charged-particle multiplicity N_C extracted from fitting azimuthal two-α-particle correlation functions, $1 + R(\Delta\phi_{\alpha\alpha})$, for α-particles emitted at $\theta = 70° - 110°$. Open and solid points represent values extracted from fits to unperturbed and perturbed correlation functions. Circular points show values extracted for energy-integrated correlation functions. Triangle and square shaped points represent results for low ($E_\alpha < E_0$) and high ($E_\alpha > E_0$) energy α-particles, respectively.

RADIAL FLOW IN Au+Au COLLISIONS at 600 MeV/A

F. Daffin, W. Bauer, and K. Haglin

Recently, experiments[1],[2] have uncovered collective and random components to the motion of light, mid-rapidity fragments from central, Au on Au collisions over a wide range of beam energies. Analysis of the light fragment spectral showed a better characterization of the motion, through χ^2-minimization, with a non-zero radial flow velocity superimposed upon a thermal distribution rather than a purely thermal distribution. This model of the motion is called the radially expanding thermal model[3], and presented the possibility of new obervables sensitive to the nuclear mean field and the in-medium nucleon cross section.

In the radially expanding thermal model, fragments are assumed to possess a thermal velocity distribution characterized by a temperature in Maxwell-Boltzmann statistics, and an overall radial velocity. In the global rest frame the resultant distribution is

$$\frac{d^3N}{dp^3} \sim \exp\left(-\gamma E/T\right)\left[\left(\frac{\gamma+T}{E}\right)\frac{\sinh(\alpha)}{\alpha} - \frac{T}{E}\cosh(\alpha)\right], \tag{1}$$

where $\gamma \equiv 1/\sqrt{1-\beta^2}$, $\alpha \equiv \gamma\beta p/T$, T is temperature and $\beta \equiv v/c$ is the radial flow velocity.

The success of BUU in reproducing the empirical radial flow and kinetic energy spectra of light composites near mid-rapidity[4] is shown in Figure 1. This success has led us to study these forms of motion over a wider rapidity range. The empirical study of Wang, et. al.[2] has shown a variation of the radial flow velocity β of deuterons as their cuts are rotated away from the major axis of the momentum ellipsoid for a given multiplicity (or average impact parameter). It is our goal find whether an increase in the sensitivity of radial flow and temperature to model parameters, such as the in-medium nucleon cross section and nuclear mean field, is realized as cuts move away from 90° relative to the beam axis. Initial theoretical considerations suggest such a realization is likely.

In our past study[4] of the phenomena, we extracted the light fragment spectra from $90° \pm 15°$ relative to the beam axis. We found the compressibility of the mean field had little effect on the radial flow, whereas the beam energy had a pronounced effect. We concluded that the the release of compressional energy stored in the mean field and, to a lesser extent, the Coulomb field to be the mechanism primarily responsible for the magnitude of the radial flow. Temperature was found to be sensitive to the beam energy, but not to the compressibility of the mean field. For central collisions, temperature was found to be sensitive to the in-medium nucleon cross section. However, this effect was appreciable for a soft (low compressibility) mean field where densities and collision rates are highest. Our current work seeks to find sensitivity in β and temperature to BUU model parameters.

In order to accomplish this, we must first establish the angle the major axis of the momentum ellipsoid makes with the beam axis. By taking advantage of our *a priori* knowledge of the reaction plane, we can safely use a two-dimensional form of the three-dimensional momentum tensor:

$$T_{ij} = \sum_{\nu=1}^{N} \frac{P_i^\nu P_j^\nu}{2m_\nu}, \tag{2}$$

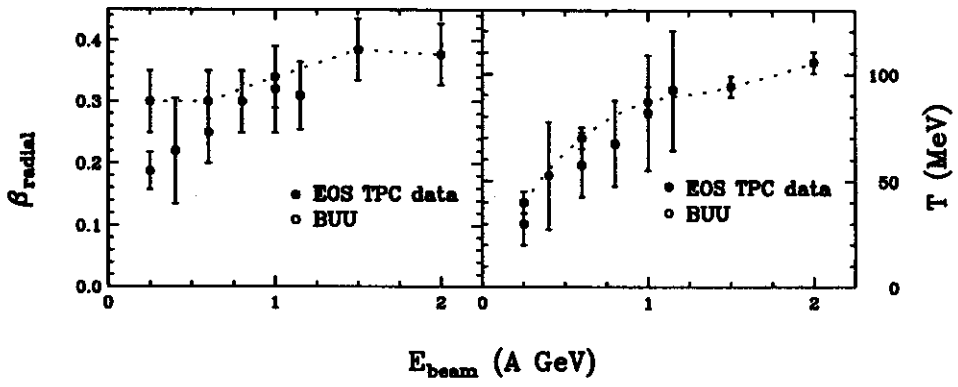

Figure 1: Excitation function of the radial flow velocity β and temperature.

BUU		EOS[2]	
θ	$b(fm)$	θ	$b(fm)$
35°	2	31°	2.3
21°	4	24°	4.3
12°	6	17°	6.1

Table 1: Angles of the major axes of the momentum ellipsoids for the BUU model and the EOS–TPC data at 600MeV/A.

where N is the total number of fragments, ν is the fragment index and i and j are Cartesian indices.

The diagonalization is then trivial, and preliminary results show good agreement with the EOS[2] efforts. The EOS collaboration extracted their average impact parameters by matching event multiplicities to QMD simulations. Thus, the EOS collaboration presents average impact parameters, whereas our results are shown without any weighting.

The next step will be to rotate the events in momentum space so that the major axis of the momentum tensor coincides with the beam axis. Finally, our simple coalescence model[4] will be imposed on the resulting single nucleon distribution and the deuteron spectra extracted for study.

Since our BUU has no self-consistent provision for the production of light fragments, a coalescence algorithm is needed to convert the phase-space distribution of protons and neutrons at freeze-out into single nucleons and light composites. Deuterons are formed whenever a proton and a neutron were within a critical radius in configuration space and the same proton and neutron are within a critical radius in momentum space. In the past these critical radii were fixed by minimizing the difference between the final-state proton spectra from BUU calculations and that from past work of the EOS collaboration[1]. We found $\Delta R_{deuteron} = 1.5\,\mathrm{fm}$ and $\Delta P_{deuteron} = 100\,\mathrm{MeV}/c$. Critical radii for heavier fragments were simply increased according to $R_i \propto A_i^{1/3}$, where i is the fragment species.

References

1. M. A. Lisa, *et. al.*, Phys. Rev. Lett. 75, 2662, (1995).
2. S. Wang, et. al., Phys. Rev. Lett. 76, 3911, (1996)
3. P. J. Siemens, J. O. Rasmussen, Phys. Rev. Lett. 42, 880 (1979).
4. F. Daffin, K. Haglin, W. Bauer, Phys. Rev. C, 54, 1375, (1996)

ISOSPIN DEPENDENT MULTI-FRAGMENTATION IN ^{112}Sn+^{112}Sn AND ^{124}Sn+^{124}Sn COLLISIONS

G. Kortemeyer, W. Bauer, and G. J. Kunde

Percolation models have proven highly successful in the simulation of multi-fragmentation reactions in the past [1,2]. Within these models, fragmentation is described by first distributing a set of points or sites, each representing a nucleon, on a 3-dimensional lattice, which represents the bonds between the sites. In the case of a simple rectangular lattice, each site is connected to six nearest neighbors, however, it has been shown that the model is to a large degree independent of the lattice structure [1,3]. In the second step, randomly some lattice bonds are broken with a probability that in non-isospin dependent percolation models is the only free parameter. The remaining connected clusters are identified with the fragments of the reaction, the bond-breaking probability with the excitation energy per nucleon [4].

The question in this work is whether the isospin-dependence found in the comparison between experimental multi-fragmentation data of ^{112}Sn+^{112}Sn and ^{124}Sn+^{124}Sn collisions [5] can be reproduced within the framework of percolation simulations. Again, we especially focus on the average number of intermediate mass fragments (IMFs, $3 \leq Z \leq 20$) versus the number of charged particles (Figure, left panels), $\langle N_{\mathrm{IMF}} \rangle (N_c)$, and versus the number of neutrons (Figure, right panels), $\langle N_{\mathrm{IMF}} \rangle (N_n)$. The full circles denote the experimental results for the ^{124}Sn+^{124}Sn reaction, the open circles the results for the ^{112}Sn+^{112}Sn reaction. The striking feature about these distributions is the "splitting" of $\langle N_{\mathrm{IMF}} \rangle (N_c)$, and the position of the maxima in $\langle N_{\mathrm{IMF}} \rangle (N_n)$. Both do not agree with common multi-fragmentation models, in which the distributions $\langle N_{\mathrm{IMF}} \rangle (N_c)$ should lie on top of each other, and the positions of the maxima in $\langle N_{\mathrm{IMF}} \rangle (N_n)$ should simply correspond to the ratio of neutron abundances in the respective isotopes.

In our simulation, we took into account fragment stability considerations. Fragment stability is achieved through fission and evaporation mechanisms.

The top row of the figure shows the result of a simulation with a bond-breaking probability distribution centered around $p_0 = 0.7$ and a half-width of 0.1. In this simulation, no stability mechanism is applied. The solid line corresponds to the simulation for the heavier isotope (experimental data indicated by full circles), the dashed line to the lighter isotope (open circles).

The second row of the figure shows the outcome of a simulation with an evaporation mechanism to achieve fragment stability: protons and neutrons are broken off the fragments until the remainder is stable. In the simulation shown, in case of $N > Z$, neutrons are broken off, and vice versa. In another simulation, protons and neutrons had been broken off randomly, which lead to slightly less IMFs.

The third row of the figure results from a simulation of a fission mechanism: an unstable fragment is broken into two fragments, if such a secondary fragment is unstable, it is again broken up into two fragments, and so on, until only stable fragments remain.

The forth row finally shows the result for a combination of the two mechanisms above, each unstable fragment undergoes evaporation or fission with equal probability. Apparently, this mechanism produces too many light fragments, both charged particles and neutrons.

In conclusion, the experimental results could only be reproduced in part. The main discrepancies are:

- The difference between the two isotopes in $\langle N_{\mathrm{IMF}} \rangle (N_c)$ could not be reproduced. This was found to be independent of fragment-stability considerations.

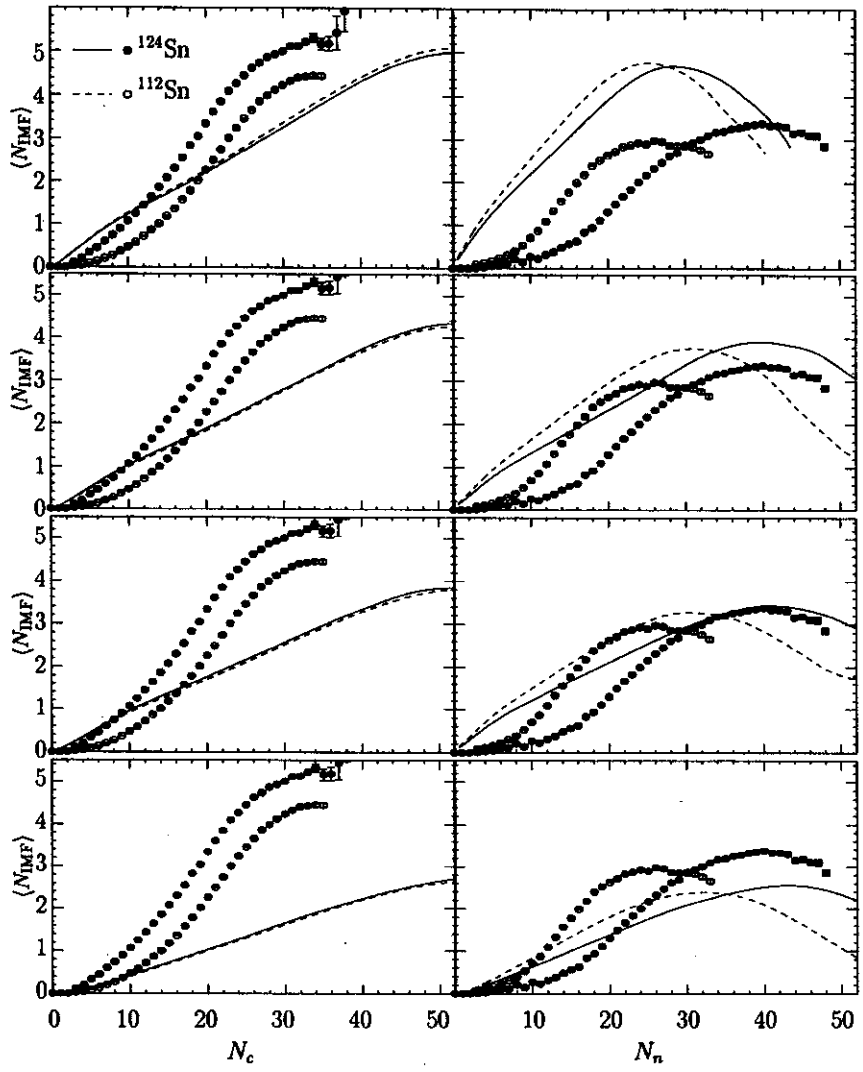

Figure 1:

- The difference in the maximum values of $\langle N_{IMF} \rangle (N_n)$ could not be reproduced.
- The experimental positions of the maxima in $\langle N_{IMF} \rangle (N_n)$ is incompatible with the simple shifting due to higher neutron abundance that is found in the simulation.

The discrepancies found between the data and this basically geometrical approach indicate that effects outside of percolation theory are important. The nuclear structure of the fragments as well as sequential feeding might play a role. Most important however seems the role of preequilibrium emission which may not only effect the sorting axis but as well determines the N/Z composition of the fragmenting system.

References

1. W. Bauer, D. R. Dean, U. Mosel, and U. Post, in *Proceedings of the 7th High Energy Heavy Ion Study* (Report GSI-85-10, October 1984), 701;
W. Bauer, D. R. Dean, U. Mosel, and U. Post, Phys. Lett 150B (1985), 53;
W. Bauer, U. Post, D. R. Dean, and U. Mosel, Nucl. Phys. A452 (1986), 699;
W. Bauer, Phys. Rev. C38 (1988), 1297;

W. Bauer and A. Botvina, Phys. Rev. C52 (1996), R1760.
2. X. Campi and J. Debois, in *Proceedings of the 23rd Bormeo Conference* (Ricerca Scientifica et Educatione Permanente, Milano, 1985), 497;
T. S. Biro, J. Knoll, and J. Richert, Nucl. Phys. A459 (1986), 692;
X. Campi, J. Phys. A19 (1986), L917;
J. Nemeth, M. Barranco, J. Debois, and C. Ngô, Z. Phys. A325 (1986), 347;
J. Debois, Nucl. Phys. A466 (1987), 724;
C. Cerruti, J. Debois, R. Boisgard, C. Ngô, J. Natowitz, and J. Nemeth, Nucl. Phys. A476 (1988), 74;
S. Das Gupta, C. Gale, and K. Haglin, Phys. Lett. 302B (1993), 372.
3. D. Stauffer, Phys. Rep. 54C (1979), 1;
J. W. Essam, Rep. Prog. Phys. 43 (1980), 883.
4. A. Coniglio, H. E. Stanley, and W. Klein, Phys. Rev. Lett. 42 (1979), 518;
D. W. Hermann and D. Stauffer, Z. Phys. B44 (1981), 339.
5. G. J. Kunde et al., Phys. Rev. Lett 77 (1996), 2897.

CORRELATIONS IN NUCLEAR ARRHENIUS-TYPE PLOTS

M. B. Tsang and P. Danielewicz

Recently, Arrhenius-type plots have been used to study the statistical [1-3] and dynamical [4] properties of fragment emissions in heavy ion reactions. Several experiments [1-3] gave evidence that in collisions characterized by a given value of the total transverse energy of detected charged particles,

$$E_t = \sum_i E_i \sin^2 \theta_i, \tag{1}$$

the IMF multiplicity distribution may be fitted by a binomial distribution,

$$P_n^m = \frac{m!}{n!(m-n)!} p_b^n (1-p_b)^{m-n}, \tag{2}$$

where n is the IMF multiplicity and the parameter m is interpreted as the number of times the system tries to emit a fragment. The probability of emitting fragments can be reduced to a single particle emission probability p_b for true binomial distributions; the binomial parameters m and p_b are related to the mean and variance of the fragment multiplicity distributions according to:

$$\langle n \rangle = m p_b \tag{3}$$

$$\sigma_n^2 = \langle n \rangle (1-p_b) \tag{4}$$

The past investigations found a simple linear relationship between $\ln(1/p_b)$ and $1/\sqrt{E_t}$ (nuclear Arrhenius-type plots), for several projectile-target combinations and incident energies[1-3]. By assuming a linear relationship between $\sqrt{E_t}$ and temperature T and from the linearity of the observed $\ln(1/p_b)$ vs $1/\sqrt{E_t}$ plot, it has been inferred that a thermal scaling of the multifragment processes might be a general property [1-3]. In this picture, the observed "linear" dependence of $\ln(1/p)$ upon $1/T$ would be reflecting the

$$p \propto \exp(-B/T) \tag{5}$$

dependence of fragment emission probabilities upon a common fragment emission barrier B. Since p and T were not measured directly in Refs. [1-3], the validity of the Arrhenius-type plots relies on two assumptions: 1) that E_t is proportional to the excitation energy E^*, and therefore, should be proportional to T^2, and 2) that p_b obtained by fitting the fragment multiplicity distributions is the elementary emission probability p.

The assumption that temperature is proportional to the square root of the excitation energy, $T \propto \sqrt{E^*}$, is valid for compound nuclei formed at low to moderate temperature. Some relationship between the transverse energy and excitation energy and therefore temperature may also be obtained for compound nuclei, provided adjustment is made for the Coulomb barrier and for neutron emission[5]. For the intermediate-energy heavy ion reactions such as $^{36}Ar + ^{197}Au$ at $E/A = 35$ to 110 MeV, where linearity of the Arrhenius-type plots have been observed, however, the final states contain fast particles emitted from the overlap region of projectile and target as well as delayed emission from projectile- and target-like

residues. In particular, particle production from the overlap participant region dominates in central collisions[6], and the transverse energy from this region is strongly affected by the collective motion[7]. There has never been any unambiguous experimental evidence supporting that $\sqrt{E_t}$ is proportional to the temperature and in fact the evidence is to the contrary. Recent temperature measurements using both the excited states populations and isotope yield ratios show that the temperature dependence on the impact parameter determined from charge particle multiplicities is very weak[8], less than 1 MeV from peripheral to central collisions. Similar trends have also been observed for the $Ar + Au$ reactions at $E/A = 35MeV$[9]. Since E_t is strongly impact parameter dependent [10], these temperature measurements thus imply that E_t is independent of temperature and the assumption that $T \propto \sqrt{E_t}$ is not valid. Based on this argument alone, the $\ln(1/p_b)$ vs $1/\sqrt{E_t}$ plot is not the Arrhenius plot analogous to that observed in chemical reactions.

Next, we will examine the assumptions used to extract the fragment emission probability. There is no apriori reason for the emitted fragments to prefer binomial statistics or Poissonian statistics. In Poissonian statistics, the probability of emitting n fragments is

$$P_p(n) = \frac{\lambda^n}{n!}e^{-\lambda} \tag{6}$$

where $\lambda = \langle n \rangle$ is the mean. For Poisson Distributions the ratio of the variance to the mean, $\sigma^2/\langle n \rangle$=1 and < 1 for binomial distribution. It has been demonstrated that constraints from conservation laws reduce the width of the Poisson distributions to much less than 1 [11]. For example, if charge conservation constraint is applied to a Poissonian distribution, Eq. (6) is modified to [12]

$$P_m(n, \alpha) = \frac{\lambda^n}{n!}e^{-\lambda}e^{-\alpha(n-\lambda)^2} \tag{7}$$

where α is the charge constraint factor.

For small α, the mean fragment multiplicity for Eqs. (6) and (7) are nearly the same; $\langle n \rangle \approx \lambda$. Fig. 1 shows three modified Poisson distributions of Eq. (7) (solid and open points) for $\lambda = 3$, 6 and 10 and $\alpha = 0.1$. To illustrate that distributions such as Eq. (7) whose values of $\sigma^2/\langle n \rangle$ are less than 1 can be described by binomial distributions, we used Eqs. (3) and (4) to determine the binomial parameters m and p_b whose values are listed in Fig. 1. The solid and dashed lines are binomial distributions of Eq. (2). The agreement between the two distributions is very good. However, in this context, m and p_b are mainly fit parameters used to describe the modified Poisson distributions of Eq. (7) and p_b is not an elementary emission probability. If the small values of $\sigma^2/\langle n \rangle$ reflect the constraints of conservation laws of Eq. (7) observed in Ref. [11], the reducibility of fragments emission to binomial distributions shown by Refs. [1-3] does not imply any fundamental significance for the parameters m and p_b thereby extracted.

Even though the $\ln(1/p_b)$ vs $1/\sqrt{E_t}$ plots constructed in heavy ion reactions are not true Arrhenius plots, analyses of many systems [1-3, 13] suggest that the approximate linearity of such plots may be universal. To explain this appealing systematics, we examine the correlations between the observable E_t, parameter p_b, and the fragment multiplicity n [13]. The binomial fit parameter m is nearly constant as a function of the transverse energy E_t [1-3]. Since E_t is obtained from the measured energies of both the light particles and fragments, from Eq. (1), the energy and multiplicities are related by

$$E_t \approx (N_C - \langle n \rangle)E_t^{LP} + \langle n \rangle E_t^{IMF}, \tag{8}$$

where N_C is the total charge particle multiplicities, E_t^{LP} and E_t^{IMF} are the average transverse energy of a

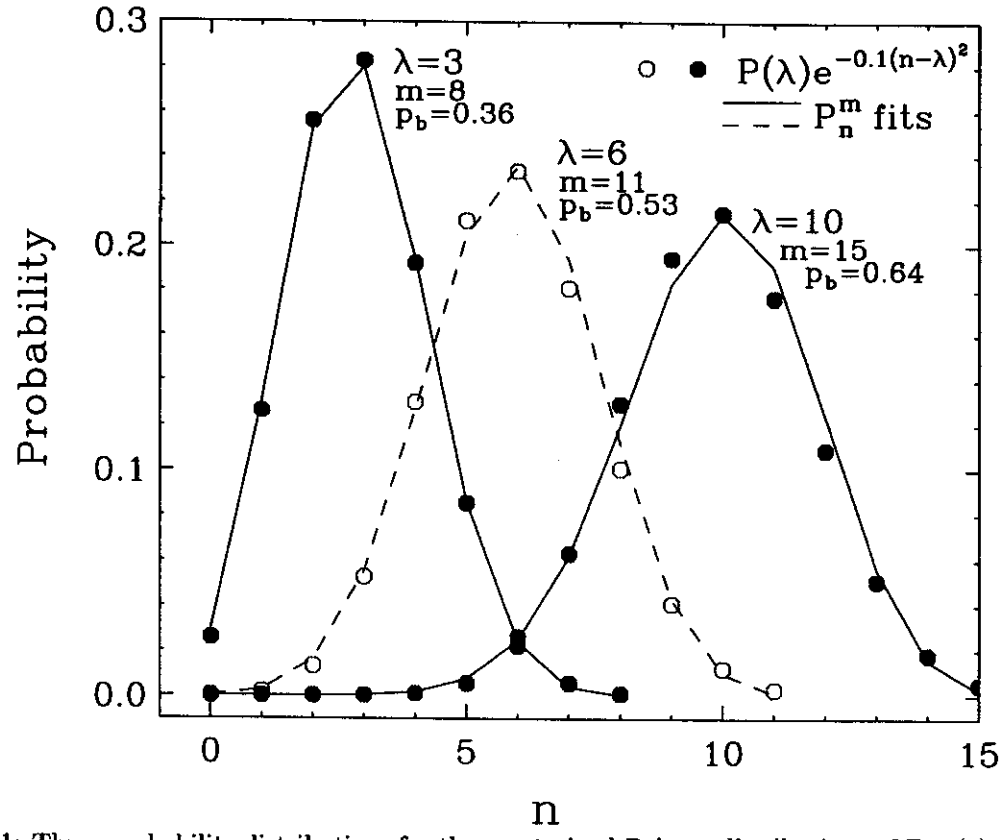

Figure 1: Three probability distributions for the constrained Poisson distributions of Eq. (7), for $\alpha = 0.1$, $\lambda = 3$ (solid points), $\lambda = 6$ (open points) and $\lambda = 10$ (solid points). The solid and dashed lines are fits with the binomial distributions, Eqs. (2-4). The corresponding fitting parameters, m and p_b are listed in the figure.

light particle and an IMF, respectively. Experimentally, the dependence of N_C on $\langle n \rangle$ can be approximated by [6]

$$N_C = a' + b'\langle n \rangle \tag{9}$$

where a' corresponds to the typical number of light charge particles emitted before any IMF is emitted and b' is the number of light charge particle emitted for each IMF emitted. Except for very large and small values of N_c, Eq. (8) can be then rewritten into:

$$E_t = a + b\langle n \rangle = b(a/b + \langle n \rangle) \tag{10}$$

where $a = a' E_t^{LP}$ is the threshold transverse energy associated with light particles emitted before any IMF and $b = (b' - 1)E_t^{LP} + E_t^{IMF}$.

To illustrate the self-correlation effect in nuclear Arrhenius-type plots, the published data for the $Ar + Au$ collisions at $E/A = 110$ MeV [1] are plotted as solid points in Fig. 2. The solid line is the self-correlation of $1/\langle n \rangle$ and $1/\sqrt{a/b + \langle n \rangle}$, scaled according to Eqs. (3) and (10) using the experimental determined values of $m = 12$ [1], $a/b = 0.5$, $b = 213$ MeV [1, 13]. The good agreement between the data and the self correlation confirms that the linearity observed in the Arrhenius-type plot mainly comes from the linear dependence of E_t on $\langle n \rangle$ of Eq. (10).

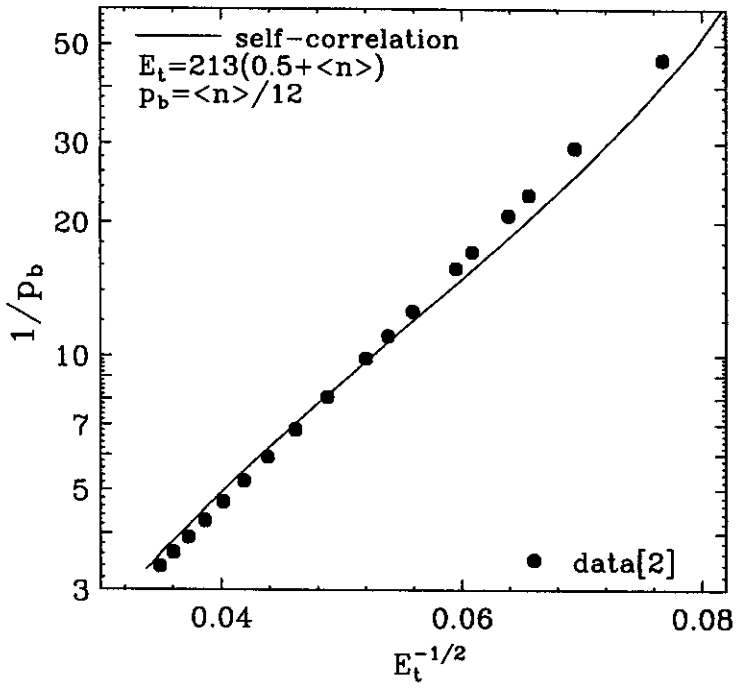

Figure 2: Arrhenius-type plot for the $Ar+Au$ reaction at $E/A = 110$ MeV [1]. The solid line is the self-correlation of $1/\langle n \rangle$ as a function of $1/\sqrt{0.5 + \langle n \rangle}$ scaled according to Eqs. (3) and (10) with the experimental values of m=12, b=213 MeV [1,13].

References

1. L. G. Moretto et al., Phys. Rev. Lett. 74, 1530 (1995).
2. K. Tso et al., Phys. Lett. B361, 25 (1995).
3. L. G. Moretto, R. Getti, L. Phair, K. Tso and G. J. Wozniak, LBL 39388 (1996), submitted to Phys. Rep.
4. J. Toke, D. K. Agnihotri, B. Djerroud, W. Skulski, and W.U. Schroder, University of Rochester preprint, submitted to PRC Rapid Communications.
5. A. Chbihi et al., Phys. Rev. C43, 666 (1991).
6. L. Phair et al., Phys. Lett. B285, 10 (1992).
7. R. deSouza, Phys. Lett. B300, 29 (1992).
8. M. J. Huang et al., Phys. Rev. Lett. 77, 1648 (1997)
9. F. Zhu et al., Phys. Lett B. 282, 299 (1992).
10. L. Phair et al, Nucl. Phys. A548, 489 (1992).
11. L. Phair et al., Phys. Lett. B291, 7 (1992).
12. M.B. Tsang and P. Danielewicz, MSU preprint, MSUCL-1069, (1997).
13. L. Phair et al., PhD Thesis, Michigan State University (1993)
14. W. Skulski et al., proceedings of 13th Winter Workshop on Nuclear Dynamics, Marathon, Fl, Feb 2-7, (1997).

PARTONS IN PHASE SPACE

David A. Brown and Pawel Danielewicz

Primary hadronic collisions in a typical nuclear collision at RHIC will occur at $\sqrt{s} \sim 200A$ GeV. Such a collision is so violent that the partons, i.e. the quarks and gluons comprising the hadrons, will become deconfined. With hadronic densities exceeding the inverse volume of a typical hadron, the partons will remain deconfined, forming a quark-gluon plasma (QGP). Since transport theory descriptions of nuclear collisions have proven successful at lower energies [1, 2, 3], it is natural to attempt to describe the time evolution of the QGP using a QCD-inspired transport model. In fact, several attempts have been made [4, 5] . Such a transport model should be based on a set of coupled integro-differential transport equations describing the complete phase-space, i.e. coordinate and momentum space, evolution of the parton densities from their initial densities. In this note, we concentrate on these initial densities.

Modeling these initial densities is difficult because the QCD coupling constant, α_{QCD}, is large, making it easy for partons to split and recombine. This complication is present in QED but, because QED has a much smaller coupling constant and a simplified coupling scheme, it is much easier to deal with these effects. As a first step toward a set of initial parton phase–space densities, we consider the virtual photon [6] and virtual electron distributions of a massive point charge. The point charge plays the role of a bare valence quark in QCD. Just as the valence quark radiates gluons the point charge radiates photons. We term these gluons (or photons) the first generation of partons. Similarly, as the gluons split into quarks–antiquark pairs, the photons virtually split into electron–positron pairs. The second generation of partons are these lepton pairs. By virtue of the QCD's large coupling constant, this splitting and radiation of partons as well as parton recombination continues beyond our ability to keep track of the various generations of partons. This splitting and recombination also occurs in QED. Since $\alpha_{QED} \ll 1$, we know that the photon distribution is dominated by the first generation of partons (photons) and the electron distribution is dominated by the second generation of partons (electrons). Thus, we can track the shape of the QED parton phase–space distribution through the various generations, even though we can not in QCD.

We will first investigate the photon distribution and later we will build the electron distribution. Figure (1 a) illustrates the process of photon radiation and absorption by a pair of currents. The upper current is that of the massive point charge. The lower current is a test current for probing the photon distribution. Figure (1 b) illustrates the absorption part of the diagram separately. We can now derive the photon distribution in a manner analogous to the method used to derive the Gribov–Lipitov–Altarelli–Parisi equations [7, 8].

We derive the Effective Photon Distribution by taking the absolute square of the S–matrix for the one photon exchange process in figure (1 a) and rewriting it in terms of Wigner transformed currents and propagators [9, 10]:

$$|S_{\mathrm{AB}\to\mathrm{A'B'}}|^2 = \int d^4x \, \frac{d^4q}{(2\pi)^4} \, A_{\mu\nu}(x,q) \, J_{\mathrm{B}}^{\mu\nu}(x,q) \, .$$

Here $J_{\mathrm{B}}^{\mu\nu}(x,q)$ is the Wigner transform of current B and $A_{\mu\nu}(x,q)$ is the Wigner transform of the photon field created by the current A. $A_{\mu\nu}(x,q)$ is written in terms of the Wigner transforms of the current A and

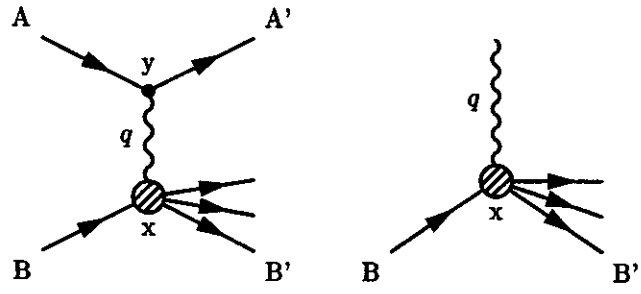

Figure 1: One photon exchange and one photon absorption. In the one photon absorption process, the photon is free.

the photon propagator:

$$A_{\mu\nu}(x,q) = \int d^4y\, D_{\mu\nu\mu'\nu'}(x-y,q)\, J_{\rm A}^{\mu'\nu'}(y,q)\,.$$

If we compare this S–matrix to the S–matrix of the one photon absorption process shown in figure (1 b),

$$|S_{\gamma {\rm B}\to {\rm B}'}|^2 = \int d^4x\, \frac{d^4q}{(2\pi)^4}\, \frac{\pi}{q_0} \sum_{\rm pol} \epsilon^{\mu}(\lambda)\, \epsilon^{*\nu}(\lambda)\, (2\pi)^4\, \delta^4(q-k)\, J_{\rm B}^{\mu\nu}(x,q)\,,$$

we can identify the virtual photon distribution. In the gradient approximation ($\partial/\partial x^{\mu} \ll q_{\mu}$), it is

$$\frac{dn_{\gamma}(x,q)}{d^4x\, d^3q\, dq^2} = \frac{q_0}{4\pi} \sum_{\rm pol} \epsilon^{\mu}(\lambda)\, \epsilon^{*\nu}(\lambda)\, A_{\mu\nu}(x,q)\,.$$

Incidentally, multiplying the photon field by the projection tensor $\sum_{\rm pol} \epsilon^{\mu}(\lambda)\, \epsilon^{*\nu}(\lambda)$ renders the photon distribution gauge invariant [11]. For the case of a massive point particle with trajectory $y_{\mu} = y_0 v_{\mu}$ and four–velocity $v_{\mu} = (1, \vec{\beta})$, where $\beta \approx c$ and $\gamma = 1/(1-\beta^2)$, we can find $A_{\mu\nu}(x,q)$:

$$A_{\mu\nu}(x,q) = \frac{32\pi^2 \alpha \gamma \delta(q\cdot v)}{\sqrt{-q^2}} v_{\mu} v_{\nu} \mathcal{A}\Big(2|x\cdot q|, 2\sqrt{-q^2\gamma^2\left((x\cdot v)^2 - x^2v^2\right) - (x\cdot q)^2}\Big)\,.$$

$\mathcal{A}(a,b)$ is the coordinate space dependent part of $A_{\mu\nu}(x,q)$. A plot of $\mathcal{A}(a,b)$ for $q_{\mu} = (m_e, \vec{0})$ photons is shown in Figure (2). The oscillations exhibited by the photon distribution are expected for a Wigner transformed density [10]. To obtain an equivalent classical distribution, one must smear this distribution over a unit volume of phase–space. Nevertheless, this distribution is clearly Lorentz contracted in the direction of the point charge's 3-momentum. Further investigation of $A_{\mu\nu}(x,q)$ shows it to be a "Lorentz contracted onion" centered on the point source. The inner layers of this "onion" correspond to higher energy energy photons. Each layer has radius $1/\gamma\sqrt{-q^2}$ in the $\vec{\beta}$ direction and radius $1/\sqrt{-q^2}$ in the transverse direction.

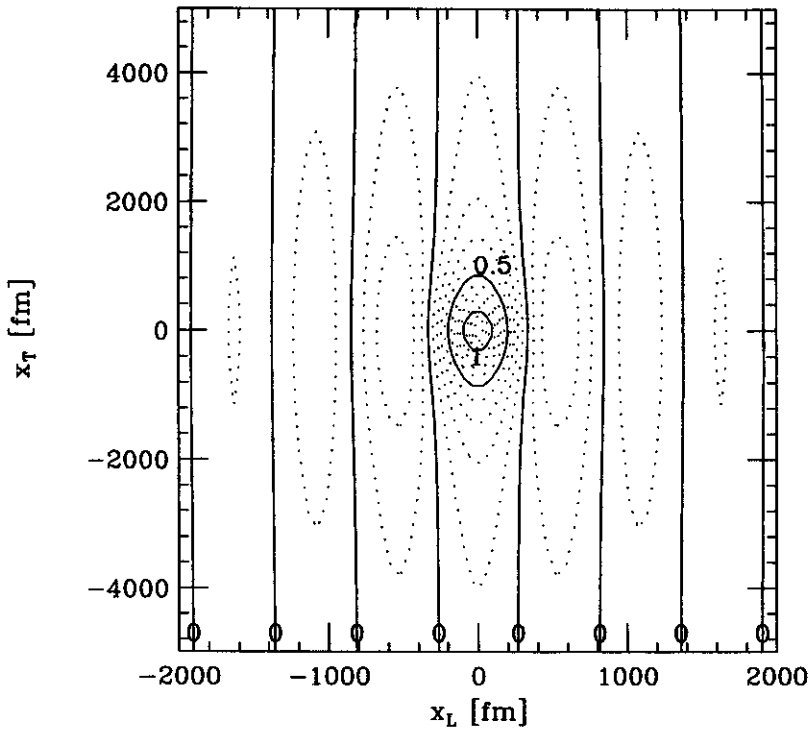

Figure 2: The virtual photon distribution of a point charge with 3-velocity $\vec{\beta}$. The photons in this slice of the full phase–space distribution have $q_\mu = (m_e, \vec{0})$.

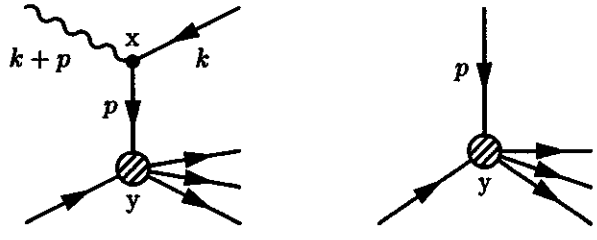

Figure 3: On the left, an electron–positron pair is created by photon splitting. The electron is absorbed by the lower probe particle. On the right, a free electron is absorbed by the probe particle.

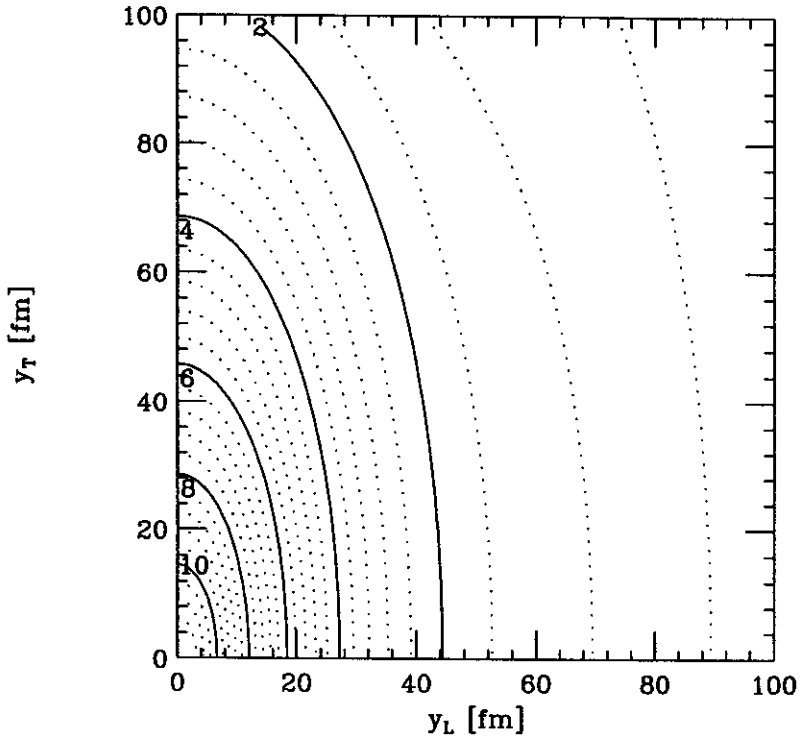

Figure 4: Coordinate space distribution of $p_\mu = (2, 1, 2, 0)$ MeV/c electrons. The distribution is symmetric, so only the upper right quadrant is shown.

We can define the virtual electron distribution in a similar manner. First we write the diagram for a photon splitting into an electron–positron pair. The resulting electron distribution is probed with another particle, such as shown in figure (3). The lower half of the diagram can be factorized in a manner analogous to the photon. The piece of the resulting electron distribution that depends on coordinate space is:

$$\frac{dn_{e^-}(y,p)}{d^4y\, d^3p\, dp^2} \propto \alpha \int d^4x \, \frac{d^3k}{2k_0(2\pi)^3} \, A_{\mu\nu}(x, k+p)\, G_{\alpha\beta\alpha'\beta'}(x-y, p)$$

Here $G_{\alpha\beta\alpha'\beta'}(x,p)$ is the Wigner transform of the electron's propagator [9]. The integral over d^3k is over the positron's on–shell momentum because we are integrating out the final state positron. We can perform this integral numerically. For massive ($m_e \neq 0$) space–like electrons with 4-momentum $p_\mu = (2, 1, 2, 0)$ MeV/c we obtain the electron distribution shown in figure (4). Because the electron is massive, it can not travel far from the central point charge. Thus, its distribution is only marginally wider than the underlying photon distribution. The radius in the transverse direction is $1/\sqrt{< -q^2 >} = 1/\sqrt{-(m^2 + p^2 + 2 < k \cdot p >)}$ where $< \cdots >$ indicates an average over the positron momentum. The longitudinal direction is again contracted by the factor $1/\gamma$.

From this analysis, we can extract several pieces of information about the initial phase–space parton densities. First, gluons spawned by a bare quark (via $q \to qg$) should be spread out in a Lorentz contracted sphere with higher energy quarks distributed closer to the source quark. The spread of the gluon distribution is given by the virtuality of the gluons in question, i.e. the radius of the distribution is $1/\sqrt{q^2}$. Second, we see that subsequent generations of partons also have Lorentz contracted distributions. For a second generation of space–like massive particles, the radius of the distribution is given by

$1/\sqrt{-(m^2+p^2+<k\cdot p>)}$. We currently are working on finding the massless electron distribution for comparison. This will be a more realistic model of quarks as quarks are usually taken to be massless. We are also deriving equations that describe the all orders behavior of the parton densities. These equations are the phase–space analog of the Gribov–Lipitov–Altarelli–Parisi equations.

References

1. P. Danielewicz, Ann. Phys. 152 (1984) 239.
2. S. Mrówczyński and P. Danielewicz, Nucl. Phys. B342 (1990) 345.
3. S. Mrówczyński and U. Heinz, Ann. Phys. 229 (1994) 1.
4. K. Geiger, Phys. Rev. D 46 (1992) 4965.
5. H. Elze and U. Heinz. Phys. Rep. 183 (1989) 81-135.
6. J.D. Jackson. *Classical Electrodynamics.* John Wiley and Sons, New York (1975). pp. 668-669, 719-725.
7. G. Altarelli and G. Parisi, Nucl. Phys. B126 (1977) 298.
8. C. Quigg. *Gauge Theories of the Strong, Weak and Electromagnetic Interactions.* Addison-Wesley, New York (1983).
9. E.A. Remler, Ann. Phys. 202 (1990) 351.
10. P. Carruthers and F. Zachariasen, Rev. Mod. Phys. 55 (1983) 245.
11. V.M. Budnev, et. al., Phys. Rep. 15 (1975) 181-282.

SIMULATIONS OF RHIC PHYSICS

J. Murray and W. Bauer

In the near future, heavy-ion colliders will go online with center of mass energies ranging from several hundred to several thousand GeV per nucleon. This increase in energy implies that the usual treatment of the individual nucleon-nucleon scattering is no longer appropriate. Distances smaller than the size of a nucleon will be probed. Therefore, simulations of these collisions must incorporate perturbative QCD to describe the subnucleonic features. HIJING, developed by Wang and Gyulassy [1], is a model of the this type which has been used to look at multiple minijet production and how it is affected by nuclear shadowing and jet quenching in pA and AA collisions.

The simulation we developed is similar to HIJING and is based on a simple prescription. The number of nucleon-nucleon collisions is determined geometrically and the individual nucleon-nucleon collisions are handled by PYTHIA and JETSET [2], typical high energy event-generators using perturbative QCD matrix elements and the Lund fragmentation scheme. Our study focuses on the effects of secondary scattering in nucleus-nucleus collisions; an effect not present within HIJING. As energies and time before freeze-out increase, one should expect collisions between produced hadrons to play a significant role in the dynamics and observables of the nucleus-nucleus collision.

Secondary scattering in our model is achieved by turning off all particle decays within JETSET. This intermediate state consists mostly of undecayed pions and rhos. These intermediate particles are allowed to scatter in a manner similar to the initial nucleon collisions, using pion parton distribution functions [3] to determine the quark structure of the mesons. Collisions between produced particles continues until the geometrically determined number of collisions is reached. At this point, all unstable particles produced are allowed to decay and the final state is formed.

A model that includes these scatterings between produced particles should also be able to reproduce lower energy data where secondary collisions are not expected to be important. With this in mind, the simulation was run for O-Au at $E_{lab} = 200$ GeV/nucleon ($\sqrt{s} \simeq 19$ GeV/nucleon) and compared to existing data for negatively charged particle rapidity distributions (left panel in Figure 1). Secondary scattering, as expected, does not contribute significantly to the particle multiplicity. When the simulation is run for Au-Au collisions at $\sqrt{s} = 200$ GeV/nucleon, the results are quite different. The pseudorapidity distributions of charged particles are displayed in the right panel of Figure 1. In this type of collision, the particle multiplicity that originates from secondary scattering is significant and increases the overall multiplicity by about 30%.

Further studies using this model into the effects of secondary scattering on other potentially useful observables in relativistic heavy-ion collisions are being discussed. Examples include J/Ψ suppression relative to Drell-Yan production and dilepton production from mini-jets.

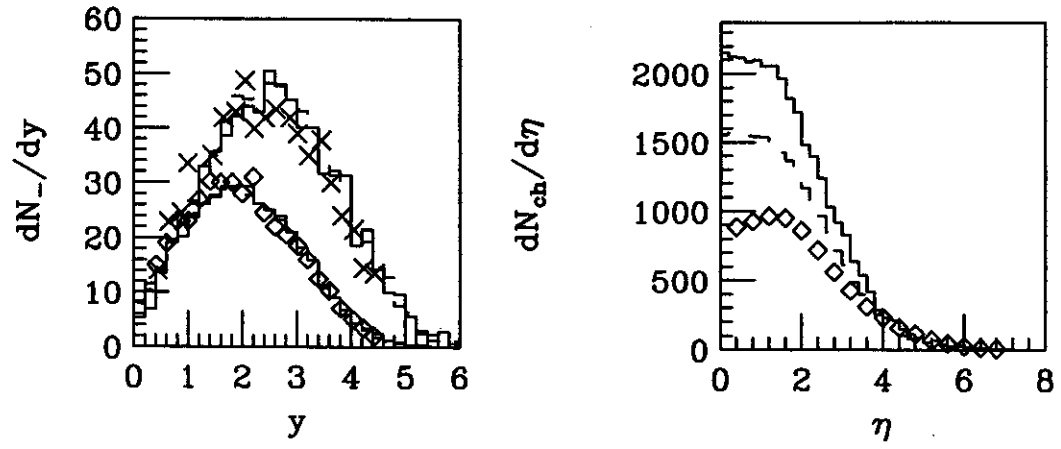

Figure 1: Rapidity distribution for O-Au from primary scattering alone (dashed-histogram) and primary plus secondary scattering (solid-histogram) compared to NA35 data [4] (right panel). Pseudorapidity distribution for Au-Au from primary scattering alone (dashed-histogram) and primary plus secondary scattering (solid-histogram) compared to HIJING data (left panel).

References

1. X. Wang and M Gyulassy, Phys. Rev. D44 (1991), 3501.
2. T. Sjöstrand, Computer Physics Commun 82 (1994) 74.
3. D.W. Duke, J.F. Owens, Phys Rev. D26 (1982) 1600.
4. NA35 Collaboration, H. Ströbele *et al.*, Z. Phys C38 (1988), 89.
5. K. Geiger and B. Müller, Nucl. Phys. B369(1992), 600.
6. G. Kortemeyer, J. Murray, S. Pratt, K. Haglin, and W. Bauer, NSCL Annual Report (1993), 63.

INVESTIGATING THE PION DISPERSION RELATION

Alexander Volya, Kevin Haglin and Scott Pratt

The pion dispersion relation in nuclear matter has long been the subject of many theoretical papers [1]. However, experimental confirmation of the expected lowering of the dispersion relation has not been fully compelling. The most insightful evidence for the energy of high momentum ($p \approx 300$ MeV/c) pions being significantly reduced comes from charge exchange experiments. In these experiments, extra strength is seen in channels where pion exchange is expected to be dominant [2].

We have studied a different reaction which is less sensitive to entrance and exit channel effects, Compton-like scattering. Through the anomalous, $\pi_0\gamma\gamma$, coupling a neutral pion can be created, but only with space-like properties, $E_\pi > k_\pi$. If the dispersion relation is sufficiently altered such that the pionic branch is pushed into the space like region, a peak in the cross-section $d\sigma/dk_\pi dE_\pi$ will be observed when the energy loss of the photon, E_π, corresponds to the on-shell energy of a pion with a momentum equal to the photon's momentum loss, k_π.

Figure 1 shows the cross-section for fixed momentum transfer k_π as a function of the energy transfer. Making this measurement only requires the observation of the outgoing photon. The cross-section is constrained to vanish at the $E_\pi = k_\pi$ boundary, which means that the peak of the dispersion relation must be more than 25 MeV below the boundary to lead to a measurable result.

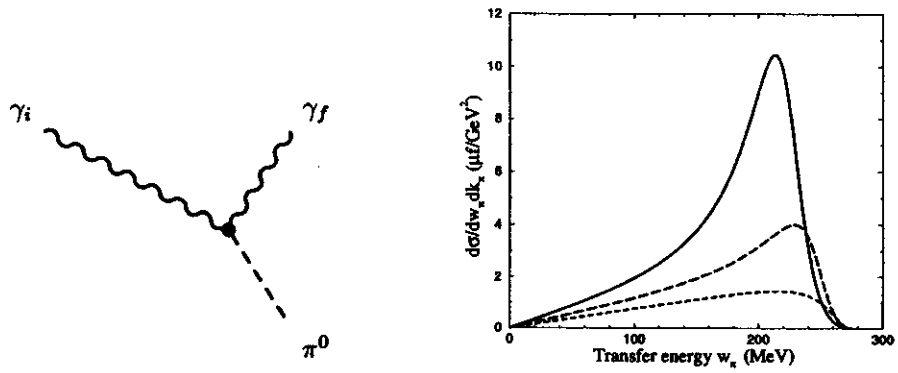

Figure 1: The cross-section for $\gamma \rightarrow \gamma\pi_0$ is shown for fixed momentum transfer $k_\pi = 275$ MeV/c as a function of the energy transfer for a lead target. The three curves represent dispersion relations, where the on-shell energies are 225 MeV, 250 MeV and 275 MeV respectively.

Figures 2 shows the diagrams used to calculate the background processes. The creation of a charged pion in a delta decay dominates the background, because light fast moving charged particles readily bremsstrahlung. Only by gating on the observation of a neutral pion, is the background decreased to a level where the peak is observed. Our results are summarized in Figure 3.

We conclude that such measurements can be powerful tools for investigating the pion dispersion relation, but that one must resign oneself to designing an experiment where the created π_0 is measured. The prospect of using polarization to decrease the background will also be reported on in a forthcoming paper.

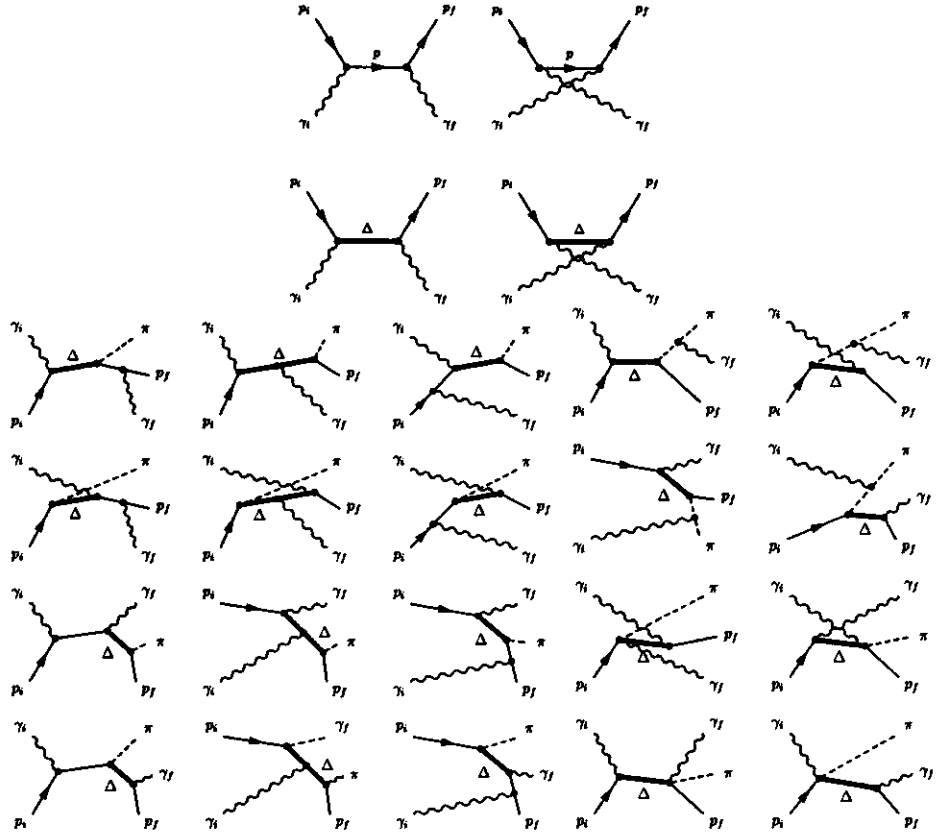

Figure 2: Feynmann diagrams for standard Compton (upper 4) and for processes where a pion is created in the final state (lower).

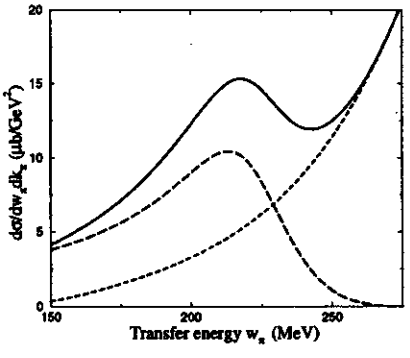

Figure 3: Background contributions where a neutral pion is created are shown with the short-dashed line. The signal, as in Figure 1, is shown with the long dashes for scattering off a lead target and assuming the on-shell energy of the pion is 225 MeV. The sum is shown with the solid line.

References

1. A. B. Migdal Rev. Mod. Phys. 50 (1978) 107.
2. V. Dmitriev Nucl. Phys. A577 (1994) 249c.

PION TRANSPARENCY IN 500 MeV PION-INDUCED REACTIONS?

Bao-An Li[a], Wolfgang Bauer, and Che-Ming Ko[a]

Pion-nucleus scatterings at energies near the peak of $\Delta(1232)$ formation ($T_\pi \approx 180$ MeV) have been studied extensively at several meson facilities during the last two decades. Experiments at LAMPF, KEK and BNL using high energy pions far above the resonance peak have recently started to accumulate interesting data[1-4]. Since the pion-nucleon cross section decreases by almost an order of magnitude as the pion energy increases from the resonance energy to higher energies, high energy pions are therefore expected to penetrate more deeply into the interior of nuclei. To understand the dynamics of these high energy pions in nuclear matter is one of the major goals of current experimental studies on pion-nucleus scatterings. These studies will be further enhanced by the availability of pion beams at GSI/Darmstadt in the near future.

Among these studies, one interesting phenomenon was recently found at LAMPF in inclusive scatterings of 500 MeV pions from a carbon target.[2] The (π, π') inclusive cross sections, with outgoing pion energies near 200 MeV, failed to show the strong depletion predicted by a intranuclear cascade model (INC)[5]. In order to approach the experimental results, it was speculated that the nuclear medium is more transparent to the pions form the $(\pi, 2\pi)$ production channel than expected from conventional physics arguments.

We studied the question of pion tranparency in our semiclassical tranport model. We found that the double differential cross sections of the 500 MeV $C(\pi, \pi')$ reaction measured at LAMPF (circles in Fig. 1) can be largely accounted for, if one uses energy-dependent, anisotropic angular distributions which are fitted to pion-nucleon scattering data for the decay of $\Delta(1232)$ and $N^*(1440)$ resonances (thick histograms).[6]

The remaining discrepancy between the data and the calculation sets a limit on effects of more exotic processes. To explore one such possibility, we increased the inelastic $\pi + N$ cross section a factor of 3, as shown by the thin histogram in Fig. 1. The agreement with data at forward pion angles and energy losses above 200 MeV is improved by using this assumption.

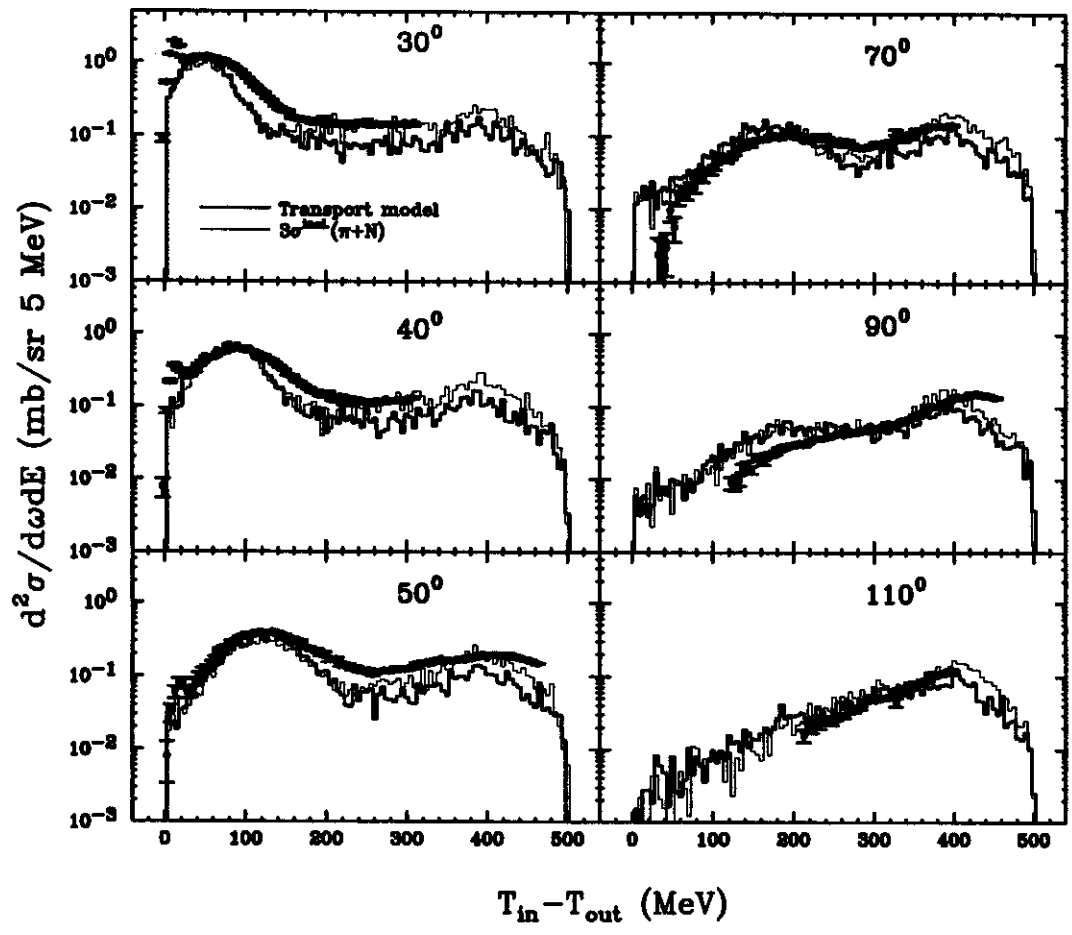

Figure 1: Inclusive double differential cross sections of pions as a function of the pion laboratory angle and the pion energy loss, $T_{\rm in} - T_{\rm out}$, in 500 MeV $C(\pi^+, \pi^{+'})$ reactions.[2,6].

a. Cyclotron Institute and Department of Physics, Texas A&M University

References

1. D. Marlow et al., Phys. Rev. C 30, 1662 (1984).
2. J.D. Zumbro et al., Phys. Rev. Lett. 71, 1796 (1993).
3. J.E. Wise et al., Phys. Rev. C 48, 1840 (1993).
4. M.W. Rawool-Sullivan et al., Phy. Rev. C49, 627 (1994).
5. W.R. Gibbs and W.B. Kaufmann, in Pion-Nucleus Physics: Future Directions and New Facilities at LAMPF, Los Alamos, New Mexico, 1987, Eds. R.J. Peterson and D.D. Strottman, AIP Conference Proceedings No. 163 (AIP, New York, 1988), P. 279.
6. B.A. Li, W. Bauer, and C.M. Ko, Phys. Lett. B382, 337 (1996).

LOW-MASS DILEPTON PRODUCTION AT THE CERN SPS

J. Murray, K. Haglin and W. Bauer

Measuring and analyzing electromagnetic radiation from heavy-ion collisions represents a significant experimental challenge compared to hadronic signals owing to the relatively small cross sections. The additional information they provide certainly justifies the undertaking. Hadrons produced in the initial stages of the collision interact on average several times before leaving the reaction zone. Consequently, any information embedded in hadronic dynamics is completely masked by multiple scatterings. Dileptons are not disturbed by the hadronic environment even though they are produced at all stages of the collisions as they have long mean free paths. They are dubbed "clean probes" of the collision dynamics.

Recent results from CERN [1]have brought about a surge of activity in search of quantitative interpretation. The proton-induced reactions (p+Be and p+Au at 450 GeV) are consistent with predictions from primary particle production and subsequent radiative and/or Dalitz decays suggesting that the e^+e^- yields are fairly well understood. Yet, the heavy-ion data (S+Au at 200 GeV/n) show a significant excess as compared to the same model for meson production and electromagnetic decays. When integrated over pair invariant mass up to 1.5 GeV, the number of electron pairs exceeded the "cocktail" prediction by a factor of 5 ± 2. It is clear that two-pion annihilation contributes in the heavy-ion reactions as fireball-like features emerge and support copious pion production [2]. Vector dominance arguments would naturally lead to extra production around the rho mass. Yet, the excess is most pronounced between the two-pion threshold and the rho mass.

The nature of the enhancement suggests several possibilities. Medium modifications resulting in a shifted rho mass could be responsible [3]. Along these lines, consequences arising from a modified pion dispersion relation have been investigated considering finite temperature effects [4] and collisions with nucleons and Δ resonances [5]. Secondary scattering of pions and other resonances has also been studied [6] focusing on the role of the a_1 through $\pi\rho \rightarrow a_1 \rightarrow \pi\, e^+e^-$. The contribution was shown to be relevant but not sufficient for interpreting the data. We extend the secondary scattering investigation in the present calculation by including non-resonance dilepton-producing $\pi\rho \rightarrow \pi\, e^+e^-$ reactions [7].

Future collider energies, several thousand GeV per nucleon in the center of mass, probe distances much smaller than the nucleon. Models must of course incorporate QCD to describe the subnucleonic features. Quarks and gluons then comprise the appropriate degrees of freedom for a QCD transport theory. They are propagated through spacetime approximating the dynamics of collisions to be explored at RHIC and LHC [8,9,10,11]. Evolution continues until soft processes dominate and hadronization occurs.

Whether or not a quark-gluon plasma can be experimentally detected depends largely on the characteristics of the collision in its absence, something we shall call background. In order to better quantify this background, simulations without "built-in" plasma formation that still assume a QCD description of nucleon scattering must be explored. HIJING, developed by Wang and Gyulassy [12], is precisely this type of model and has been used to look at multiple minijet production, shadowing and jet quenching in pA and AA collisions.

The simulation we develop is similar to HIJING. It is based on a simple prescription that uses QCD to characterize the individual nucleon-nucleon collisions and uses Glauber-type geometry to determine the scaling. The kinematics of the nucleon-nucleon collisions are handled by PYTHIA and JETSET [13], high energy event-generators using QCD matrix elements as well as the Lund fragmentation scheme.

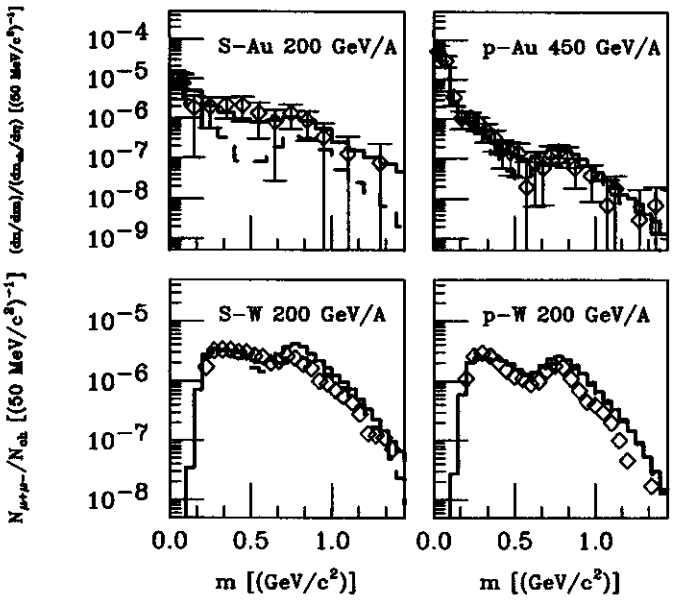

Figure 1: Dilepton invariant mass spectrum from primary scattering alone (dashed-histogram) and primary plus secondary scattering (solid-histogram). The top panels shows the comparison to CERES data for S+Au (left top panel) and p+Au (right top panel). The bottom panels show the comparison to HELIOS/3 data for S+W (left bottom panel) and p+W (right bottom panel).

The invariant mass spectra of dileptons from the initially produced mesons, such as $\pi^0, \eta, \eta', \omega, \rho, \phi$, in our model for the S+Au and p+Au systems are displayed in Fig. 1. The simulation agrees with the proton-induced data and it is reassuring that our S+Au model-results are consistent with the cocktail from the CERES collaboration [1]. Plotting against the actual S+Au data reveals a significant enhancement over predictions in the invariant mass region between 200 and 500 MeV. There is also a modest enhancement for masses above this range.

Dileptons from pion annhilation, $\pi\rho$ non-resonant and resonant scattering for the S+Au system in our model are added to those from primary scattering. The contribution from pion annihilation increases the distribution significantly in the rho mass region, but still leaves an excess below the rho mass. We should stress that we have taken vacuum rho properties throughout. Radiative a_1 decay contributes a minimal amount in the excess (or deficit) region, but the contribution from non-resonance $\pi\rho$ scattering provides the most significant increase.

The secondary scattering previously described, has been included in the invariant mass distributions of dileptons. The dilepton spectra from the proton-induced interactions are not significantly changed, Fig. 1. This result is as expected—dileptons from the smaller systems are quantitatively described by primary hadronic decays. The proton-nucleus collisions do not create a heated nuclear medium large enough or dense enough to bring about significant collective effects. Conversely, the S+Au collision has a marked increase in lepton-pair production between an invariant mass of 200 and 500 MeV as well as a noticeable increase in the higher mass region, Fig. 1. It is not surprising that secondary scattering becomes important in the S+Au system, as a dense nuclear medium is created during the collision.

As a further check to our calculations, the simulation was modified so that we could study muon

pair production and compare to HELIOS/3 [14] results, Fig. 1. The experiment measured the invariant mass distribution of muon pairs from S+W and p+W at 200 GeV. The $\pi\rho$ cross section used in our model was recalculated with muons in the final state instead of electrons and all relevant branching ratios were changed to the correct values for resonances decaying into muons. In the invariant mass region between 0.2 and 0.5 GeV, there is an excess in the S+W data over the proton-induced data, although less pronounced than in the S+Au reaction. The resulting spectra are consistent with the study of electron pairs.

Allowing for the short-comings of our model, results still suggest that secondary scattering is a viable explanation for the excess found in dilepton data. Inclusion of secondary scattering, 1) preserves the consistency the primary scattering in our model has with proton-induced data and, 2) enhances the number of dileptons within the region of excess discovered in S+Au and S+W data. Although this agreement cannot rule out other possible explanations for the excess electrons, our model's simplicity is attractive.

References

1. G. Agakichiev *et al.*, 1995, Enhanced production of low-mass electron pairs in 200 GeV/nucleon S-Au collisions at the CERN super proton synchrotron, *Phys. Rev. Lett.* 75:1272.
2. W. Cassing, W. Ehehalt, and C.M. Ko, 1995, Dilepton production at SPS energies, *Phys. Lett. B* 363:35.
3. G. Q. Li, C. M. Ko, and G. E. Brown, 1995, Enhancement of low-mass dileptons in heavy ion collisions, *Phys. Rev. Lett.* 75:4007.
4. C. Song, V. Koch, S. H. Lee, and C. M. Ko, 1996, Thermal effects on dilepton production, *Phys. Lett. B* 366:379.
5. R. Rapp, G Chanfray, and J. Wambach, 1996, Medium modifications of the rho meson at CERN/SPS energies, *Phys. Rev. Lett.* 76:368.
6. K. L. Haglin, 1996, Excess electron pairs from heavy-ion collisions at CERN and a more complete picture of thermal production, *Phys. Rev C* 53:R2606.
7. For first suggestions and preliminary results of the importance of this mechanisms, see, K. Haglin, proceedings of INT/RHIC Workshop *Electromagnetic Probes of Quark Gluon Plasma* 24–27, 1996; and proceedings of *International Workshop on Hadrons in Dense Matter*, GSI, Darmstadt, 3–5 July 1996.
8. K. Geiger and B Müller, 1992, Dynamics of parton cascades in highly relativistic nuclear collisions, *Nucl. Phys. A* 544:467c.
9. K. Geiger and B. Müller, 1992, *Nucl. Phys. B* 369:600.
10. G. Kortemeyer, J. Murray, S. Pratt, K. Haglin, and W. Bauer, 1995, Causality violation in cascade models of nuclear collisions, *Phys. Rev. C* 52:2714.
11. G. Kortemeyer, J. Murray, S. Pratt, K. Haglin, and W. Bauer, 1994, Parton cascade for RHIC, *NSCL Annual Report*, 63.
12. X. Wang, M. Gyulassy, 1991, HIJING: A monte carlo model for multiple jet production in pp, pA, and AA collisions, *Phys. Rev. D* 44:3501.
13. T. Sjöstrand, 1994, *Computer Physics Commun.* 82:74.
14. M. Masera for HELIOS/3 collaboration, 1995, Dimuon production below mass 3.1 GeV/c^2 in p-W and S-W interactions at 200 GeV/c/A, *Nucl. Phys. A* 590:93.

VIRTUAL CLUSTER STATES IN QUASIELASTIC KNOCKOUT REACTIONS

Alexander A. Sakharuk[a] and Vladimir Zelevinsky

The long-standing problem of experimental signatures for clustering effects in light nuclei is discussed for the conditions corresponding to a recent experiment [T. Yoshimura *et. al.*, private communication]. The measurements with polarized protons at comparatively low incident energy, $E_p = 296$ MeV, on the targets ^{6}Li, ^{7}Li, ^{9}Be, and ^{12}C, and at different proton scattering angles, θ_p=35°, 45° and 55°, were performed in Osaka. The specific reaction $^{12}C(p,p'\alpha)^8Be$ at incident proton energy 300 MeV and fixed proton and alpha-particle angles near the quasielastic peak is studied in detail. The Glauber approximation with a simple parametrization of the elementary nucleon-nucleon amplitude is used for calculating the cross section. The main emphasis is on the existence of virtually excited cluster configurations and their manifestation in experimental observables. The shell model wave function of the ^{12}C ground state is used to extract the weights of excited cluster components and to calculate their contributions to the cross section. The effects strongly depend on incident energy and momentum transfer and can be stressed by the choice

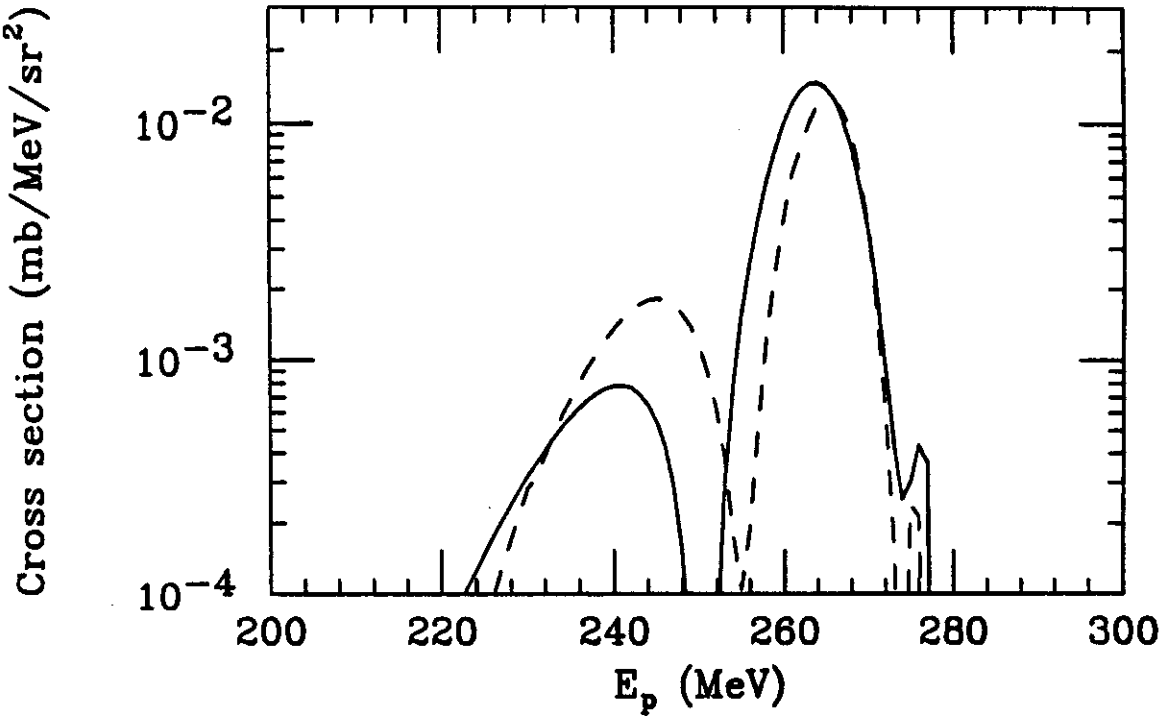

Figure 1: The presence of several excited components and their complicated interference influence the shape and the height of the quasielastic peak; the change can reach an order of magnitude, Figs. 1 and 2. The triple differential cross section of the $^{12}C(p,p'\alpha)^8Be_{g.s}$ reaction at $\theta_p = 35°$ calculated in the DWIA. The dashed line shows the contribution of the diagonal, with respect to the states of the knocked out α cluster, transitions. The solid line corresponds to all possible transitions from virtually excited states of the α cluster inside the target nucleus.

of kinematics. It is shown that the cross section for cluster emission with the excitation of ^{8}Be into the first excited 2^+ state is small as compared to the process leaving ^{8}Be in its ground state; this is important for the interpretation of experiments with limited resolution. The applicability of the Glauber approximation and possibilites for improvement are discussed. As a part of the work, all relevant two-particle and

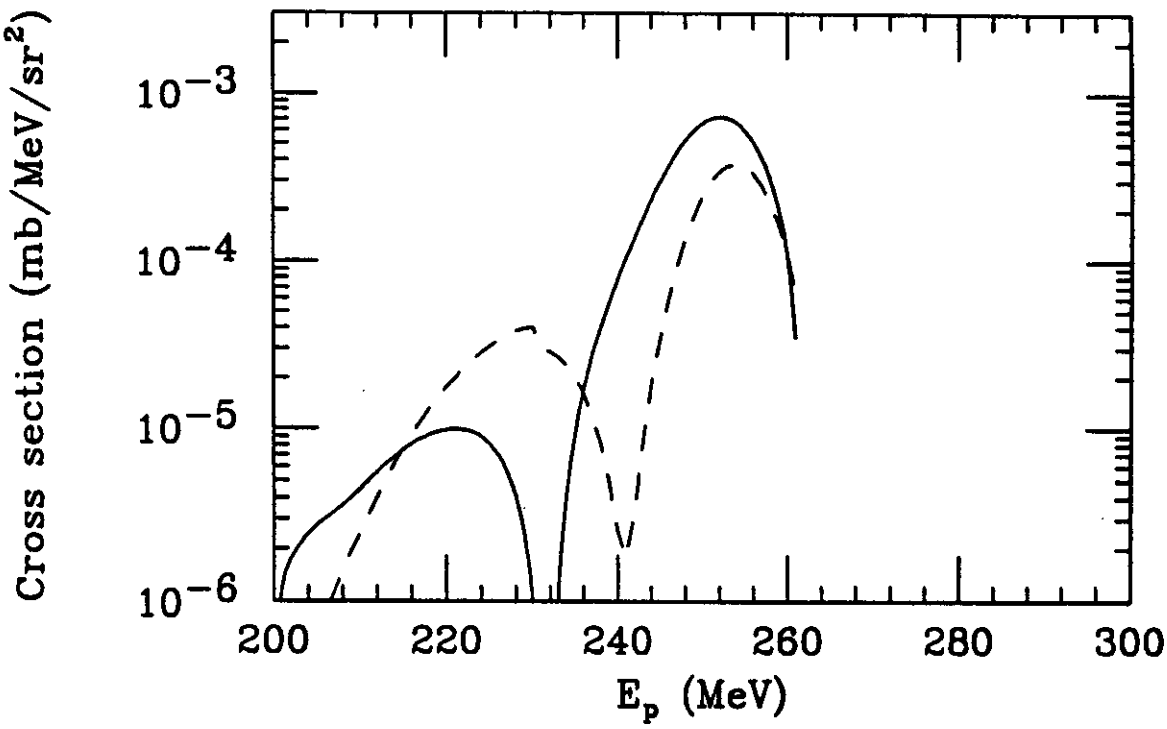

Figure 2: The presence of several excited components and their complicated interference influence the shape and the height of the quasielastic peak; the change can reach an order of magnitude, Figs. 1 and 2. The triple differential cross section of the $^{12}C(p,p'\alpha)^8Be_{g.s}$ reaction at $\theta_p = 45°$ calculated in the DWIA. The dashed line shows the contribution of the diagonal, with respect to the states of the knocked out α cluster, transitions. The solid line corresponds to all possible transitions from virtually excited states of the α cluster inside the target nucleus.

alpha-particle fractional parentage coefficients in the translationally invariant shell model are calculated.

a. Permanent address: Brest State University, Brest 224665, Belarus.